Powder Technology 429 (2023) 118940

Contents lists available at ScienceDirect

Powder Technology

journal homepage: www.journals.elsevier.com/powder-technology

Numerical study of blast wave propagation through granular materials subjected to buried blasts

Chuanshan Zhang [a], Chun Feng [b], Kun Xue [a,*]

[a] State Key Laboratory of Explosion Science and Technology, Beijing Institute of Technology, Beijing 100081, China
[b] Key Laboratory for Mechanics in Fluid Solid Coupling Systems, Chinese Academy of Science, Beijing 100190, China

HIGHLIGHTS

- Blast wave in sand coupled with gas evolution via FEM-DEM.
- Transition diagram of sand pressure profiles under blast loads.
- Correlation of peak pressure with wave propagation in blast-loaded sand.
- Analytical model predicts blast wave propagation and decay in structures.

GRAPHICAL ABSTRACT

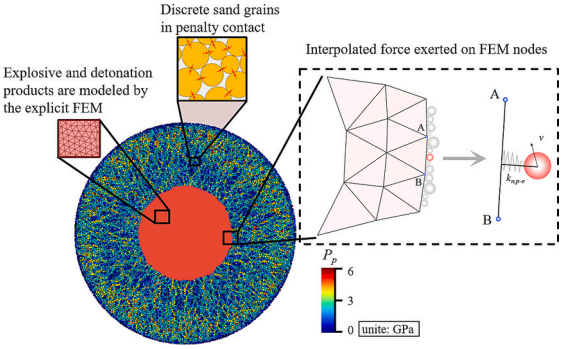

ARTICLE INFO

Keywords:
Buried blast
Pressure-profile
Granular materials
Coupled FEM and DEM
Numerical simulations

ABSTRACT

Blast wave propagation in dry sand subjected to a buried charge is numerically investigated using a charge-sand stratified configuration wherein the mass ratio between sand and charge (M/C) spans over two decades. The detonation of the central charge and the sand dynamics are modeled by the FEM-DEM method. The findings reveal the pressure-profile associated with the blast wave undergoes marked shape transition as the expansion fans catch up with the incident blast wave. The blast propagation and the associated pressure-profiles depend on the coupling between the sand and the detonation products in the central gas pocket which is in turn influenced by a variety of structural parameters. Specifically, as the M/C increases from 21 to 436, the average velocity of the blast wave decreases by 22.2%. Furthermore, a blast compaction model of sand is proposed to account for the coupling effect and justify the influences arising from key-structural parameters.

1. Introduction

Buried improvised explosive devices (IEDs) and landmines pose a major threat to both civilian and military personnel in regions of recent international conflict [1–6]. Therefore, there is an increased need for the scientific community to predict the blast loading generated when detonation products and sand ejecta impinge on a target [7–9]. When an explosive is detonated beneath the ground surface, a blast wave travels into the surrounding soil, compacting the soil skeleton as it propagates. Meanwhile, the resultant detonation products confined by the surrounding soil violently expand, accompanying a complex wave system

* Corresponding author.
E-mail address: xuekun@bit.edu.cn (K. Xue).

https://doi.org/10.1016/j.powtec.2023.118940
Received 18 March 2023; Received in revised form 6 August 2023; Accepted 23 August 2023
Available online 24 August 2023
0032-5910/© 2023 Elsevier B.V. All rights reserved.

Nomenclature

Y, G	Young's modulus, shear modulus
x, μ	damping coefficient, Coulomb friction coefficient
R, $R_{in,0}$, $R_{out,0}$	the distance to the core, the radius of TNT, the out radius of charge-sand
r_p, r_{exp}	the particle material density, explosive density
f_0, f_{comp}	initial and after compacted packing fraction
E_G	Gurney energy
V_{mean}, $V_{G,f}$	the mean velocity of sand rings/shells, the modified Gurney velocity
$\widetilde{V}_{mean}$, $V_{mean,con}$	the mean velocity and the converged mean velocity scaled $V_{G,f}$
$\langle P \rangle$	the circumferentially averaged pressure
DW, BW	the detonation wave, the blast wave
REW_h, REW_t	the head and tail of the Riemann expansion wave
TEW_h, TEW_t	the head and tail of the transmitted expansion wave
RW, SSW	the rarefaction wave, the secondary shock wave
REW_h^{inward}, REW_t^{inward}	the head and tail of the inward reflected expansion wave
$RSW^{outward}$	the outward reflected shock wave
REW_h^{inward}, REW_t^{inward}	the head and tail of the outward reflected expansion wave
t	timescale based on the velocity of the DW and the ring thickness
$\widetilde{t}$	the time is scaled by t
$\widetilde{t}_{DW}$, $\widetilde{t}_{BW}$, $\widetilde{t}_{REW_h}$, $\widetilde{t}_{SSW}$	the characteristic times of waves scaled by t
$\widetilde{r}$	the spatial coordinate is scaled by the ring thickness
$\widetilde{r}_{cr}$	the scaled distance where the TEW_t catches up with the BW
$\langle P \rangle$, $\langle u_p \rangle$, $\langle \phi_p \rangle$	the averaged particle phase pressure, particle velocity, local volume fraction
σ_{ij}^d	the quasistatic part of the total particle phase stresses
$\langle P_{peak} \rangle$, $\langle P_{d,peak} \rangle$	the peak pressure, dynamic pressure
V	the characteristic velocity
$\widetilde{\widetilde{V}}_{BW}$, $\widetilde{\widetilde{V}}_{TEW_t}$, $\widetilde{\widetilde{V}}_{RW}$	the average velocities of the BW, TEW_t and RW, scaled by V
P_p	instantaneous quasistatic pressure of particle
$\left\langle \widetilde{V}_{in} \right\rangle$	the innermost layer's velocity
$\langle P_{in} \rangle$	the gaseous pressure exerted on the inner surface
$\triangle h$	the blast front's width
$R_{out,th}^{I}$, $R_{out,th}^{II}$	the threshold of the outer radius
$\widetilde{\widetilde{R}}_{out,th}^{I}$, $\widetilde{\widetilde{R}}_{out,th}^{II}$	the $R_{out,th}^{I}$ and $R_{out,th}^{II}$ scaled by $R_{in,0}$
$D\widetilde{t}_I$, $D\widetilde{t}_{II}$, $D\widetilde{t}_{III}$	three characteristic times
$F_{\nabla P}$, F_{drag}	pressure gradient forces, drag forces
$\widetilde{R}_{in}^{pre}$, $\widetilde{R}_{BW}^{pre}$,	predicted trajectories of the inner surfaces of rings and the BW
$\widetilde{R}_{in}^{num}$, $\widetilde{R}_{out}^{num}$, $\widetilde{R}_{BW}^{num}$	the simulation derived trajectories
$P_{d,BW}^{pre}$	the analytical predicted dynamic pressure
$\overline{\left\langle P_{d,BW}^{num} \right\rangle}$	the numerically derived dynamic pressure at the blast front
Dw	the blast front has a finite width
P_s	the quasistatic pressure

that consists of the denotation front, the ensuing Riemann wave, their reflected waves off the surface between the central detonation products and the surrounding soil, the outgoing waves after the reflected waves converge into the center, etc. Since the evolution of the detonation products is fully coupled with the compaction of the surrounding soil, various waves active in the detonation products invoke their counterparts in the soil, rendering unloading and reloading cycles of the compacted soil in the wake of the outgoing blast front. Understanding this complex blast compaction process is imperative to properly assess the momentum and energy transferred from the detonation products to the surrounding soil and resultant blast loading to the target above the ground. In addition to the loading sustained by the soil skeleton during soil blast compaction directly exerted on the underground structures, predicting the pressure profiles at different distances from the charge center is necessary for evaluating the protection level for these structures.

Considerable work has been dedicated to investigating the propagation of blast waves in soil via both experimental and numerical means. Several empirical relations are also available that have been developed based on field experiments and numerical simulations. These equations provide engineers with preliminary estimations of parameters such as peak soil pressure and peak particle velocity as a function of buried explosive mass and distance, albeit their reliability has been questioned. Specifically, Leong et al. [10] found that the widely used TM5–855-1 manual (The US Army Corps of Engineers) substantially overestimates the peak pressures measured from small-scale explosion tests in Singapore residual soils. These researchers recognized that a more reliable method for estimating the attenuation coefficient is needed. As the depth of burial decreases, the peak soil pressure is increasingly affected by the ground surface, which cannot be accounted for in empirical relations. In shallow buried blast experiments, the compressive stresses transmitted through the soil skeleton are difficult to measure since the sensors mounted on the specimen are likely damaged [3].

To better assess the shock- and blast-induced dynamic pressure wave and dynamic responses of soil, an increasing number of researchers have resorted to shock tube- and shock-tube-based impulsive equipment to simulate shock or blast waves in a controlled laboratory environment [11–18]. Although their experimental work has shed significant light on the propagation and attenuation of stress waves, the acceleration and velocity response of sand particles and the dynamic strain induced in sand columns, the pressure profiles exerted on sand column surfaces do not reflect the influence arising from the evolution of detonation products confined by the surrounding sand, which is inevitable in buried blasts. In addition, the peak overpressure in these experiments is on the order of $O(10^1)$ MPa, several orders of magnitude less than the detonation pressure; therefore, the pressure rise is mainly attributed to the shock compaction of particles and the dynamic stresses due to the grain inertia effect [19]. In contrast, the overall stress state of sand subjected to a buried explosion has contributions from both quasistatic (consolidation) and dynamic (microinertia) mechanisms [20,21]. Therefore, shock tube-based experiments cannot properly approximate a buried blast.

The advent of numerical tools (such as Eulerian–Eulerian and coupled Lagrangian–Eulerian techniques), combined with the large increase in computational resources over the last decade, has allowed new insight into the complex, coupled loading processes associated with soil-blast events. Depending on whether soil is treated as a homogeneous continuum or an assembly of discrete grains, two widely used approaches are Eulerian–Eulerian and Eulerian–Lagrangian descriptions [13,14,22,23]. The Eulerian–Eulerian approach, referred to as macroscale modeling, treats both the gaseous detonation products and soil as separate continua. In the context of the buried blast where the characteristic diffusion time of gases is much larger than the characteristic time of the dynamic process, the porosity is thus deemed to be closed. Intrinsically multiphase soil is often described by a continuum model comprising contributions from both the solid matrix and interstitial

gases (and liquids). The most widely used soil material models in military communities are the so-called "porous-material/compaction" model and the Clemson University (CU) and Army Research Laboratory (ARL), USA (CU-ARL) sand model, whose parameterization was performed using a variety of experimental data as well as first-principle-type estimations [23,24]. Both models incorporate the pressure-dependent but strain rate-independent strength model. Various Eulerian hyperbolic multiphase flow models instead introduce a "configurational energy" as a function of volume fraction to describe the granular material yield strength. These constitutive relations adequately account for the consolidation (hydrodynamic) part of the stress state, which mainly dictates the soil's dynamic response when the contacts between sand particles remain semipermanent [19,25–27]. The inertial part of the stress state becomes increasingly important when the interparticle collision dominates the interaction between particles, which often occurs during the compaction of loosely packed sand and the propagation of tensile waves. In this regime, the continuum constitutive model becomes inadequate. In addition, since continuum models smooth out the heterogeneities in soil and are parameterized using standard experiments, they are insufficient to reveal the underlying physics governing the propagation and attenuation of the blast-induced dynamic pressure wave sustained by the interparticle collisions and contacts, which heavily depend on the particle-level structure. Additionally, understanding the effects of various soil properties entails particle-scale knowledge.

To resolve particle-scale dynamics, a first-principle-type method based on the Lagrangian formulation, known as the discrete element method (DEM), has been developed. In this method, each particle is tracked as a discrete entity, and individual particle behaviors can be modeled in detail. DEMs can be further categorized into nonresolved and resolved models, referred to as semi-mesoscale and mesoscale modeling, respectively. Both nonresolved and resolved models have been employed to study a variety of shock/blast-induced responses of granular materials [28]. These responses include localized phenomena, such as shock-induced heating, viscous flow or dissipation as related to hot-spot formation; the bulk material properties of porous granular systems, such as compaction density, energy deposition, zero pressure shock speed, and Hugoniot slope; and transient behaviors, such as shock formation mechanisms, propagation and attenuation of pressure waves, and detonation of energetic granular materials. Specifically, a variant of the nonresolved DEM, also known as the corpuscular method, has been successfully used to model sand ejecta resulting from shallow buried blasts [8,9,27,29,30]. The resultant close-range blast loading is consistent with the experimental results, indicating the reliability of the DEM in modeling the shallow buried blast phenomenon.

To gain grain-scale insights into the propagation of the dynamic pressure wave transmitted into sand subjected to a buried blast, we adopt the nonresolved DEM to simulate the sand, while the high explosive detonation products are modeled by the finite element method (FEM). The coupled FEM-DEM method based on a Lagrangian formulation (see Section 2) has several advantages over coupled Lagrangian–Eulerian approaches, as both advection errors and severe contact problems are avoided. This method is validated against the quasistatic uniaxial compression experiment of sand and the explosive dispersal of sand spherical shells described in Section 3. We proceed to carry out a series of FEM-DEM simulations of the buried blast using both 2D and 3D stratified configurations. Numerical details are presented in Section 4. In Section 5, the results regarding the propagation of various waves and the resultant pressure profiles are analyzed. An analytical model is proposed in Section 6 to predict the propagation of the blast front in the particle ring/shell, which yields explicit correlations between the key properties of soil and the propagation of dynamic pressure waves.

2. Numerical methods

The modeling principle is indicated in Fig. 1, whereby the momentum transfer between the expanding detonation products and discrete spherical sand grains occurs through the contacts between the outermost FEM meshes and the innermost layer of particles. This method allows for a simple, physically clear and robust treatment of the interaction between the high explosive and sand grains. The fundamentals of the coupled FEM-DEM, algorithm details and problem formulation are described in Xue et al. [31]. In this section, we only present a brief account of the computational procedure. All simulations are performed on a platform based on the Continuum-Discontinuum Element Method [32,33], which supports a range of simulation software packages for various physics and engineering applications, especially coupled phenomena and multiphysics [34].

Similar to the corpuscular method, the FEM-DEM approach treats sand particles as rigid spheres whose contacts are described by a soft-sphere DEM model. The interaction between two sand particles is approximated by two linear springs, one acting in the normal direction

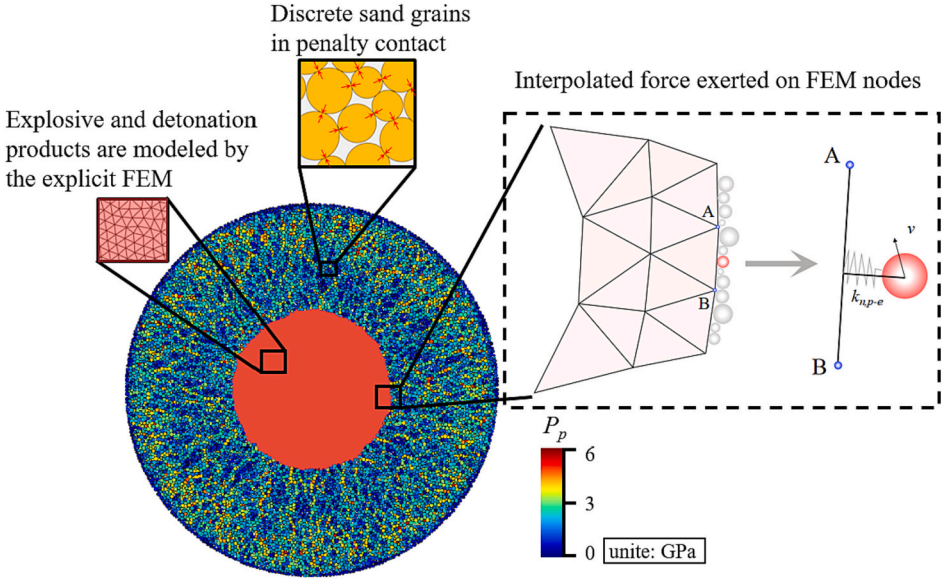

Fig. 1. Schematic of the modeling principle to explore the momentum transfer between the expanding detonation products and discrete spherical sand grains of cylindrical particle shells driven by the detonation of the central burster.

and one in the tangential direction, i.e., k_n and k_t, respectively. The effective normal and tangential stiffnesses are calculated from the Young's modulus (Y) and shear modulus (G) of particles in contact, respectively. In addition, a linear dashpot with a damping coefficient (x) acts in parallel with the normal contact spring to account for energy dissipation during the nonelastic collision. Furthermore, the tangential spring force is limited by the Coulomb friction coefficient (m). To reduce the computational cost, the soil particles are only given translational degrees of freedom. The fracture process dissipates very little energy (~2%) and is therefore not incorporated in the DEM model.

The soft-sphere DEM modeling of soil should be acceptable as long as the sand particle parameters (stiffness, damping, friction and initial packing) can be tuned such that the aggregate behaves correctly. To this end, we performed a quasistatic uniaxial compression test of sand assemblies. By comparing the axial stress vs. strain curves obtained from experiments and simulations with varying parameters, the set of sand particle parameters that yields the most comparable result is determined. In the uniaxial compression experiments, the dry sand column ($D = 80$ mm, $h = 5$ mm) consists of small silicon-based glass spheres with diameters ranging from 400 to 800 mm and a mean value of 550 mm. The density of the glass material is 2700 kg/m^3. The initial solid volume fill fraction was 60%, which gives an initial sand density of 1620 kg/m^3. In the simulations, scaled-down sand columns are confined in a cylindrical container with the same height-to-diameter ratio h/D. The size range of particles, material density and volume fraction are kept consistent with those in the experiments. To approximate the quasistatic loading condition, we gradually apply a small displacement to the top layer of particles as slowly as possible, with strain rate 10^{-3}/s. At any time step, the overall strain of the assembly (e_{zz}) is well defined by the imposed displacement, and the stress (s_{zz}) can be calculated using the averaging techniques of Satake. Fig. 2 shows the simulated results from different combinations of (Y, m) and the experimentally measured curve. The combination of Y = 78 GPa and m = 0.7 yields the compression behavior most consistent with the experimental result. Thereafter, Y = 78 GPa (G = 32.5 GPa) and m = 0.7 are used in the simulations. The damping coefficient x does not affect the quasistatic compression behavior of sand, whose value is left to be determined later in Section 4.

The corpuscular method employs the discrete particle model to simulate high explosive detonation products and air. Each particle represents a collection of 10^{15}–10^{20} molecules and follows the kinetic theory of gases, originally derived by Maxwell. The major problem with applying the corpuscular method to model detonation is that the ideal gas assumption deviates from the equations-of-state (EOSs) of the detonation products, such as the Jones–Wilkins–Lee equation-of-state (JWL-EOS). To avert this limitation, we adopt the explicit FEM to model the conversion of the solid explosive to gaseous detonation products and product expansion. The solid explosive and gaseous detonation products are described by the Mohr–Coulomb ideal elastic–plastic material model and the JWL EOS, respectively. As indicated in Section 5, the detonation of a solid explosive simulated by the explicit FEM yields a wave system in the gaseous detonation products consistent with that obtained via Eulerian formulation.

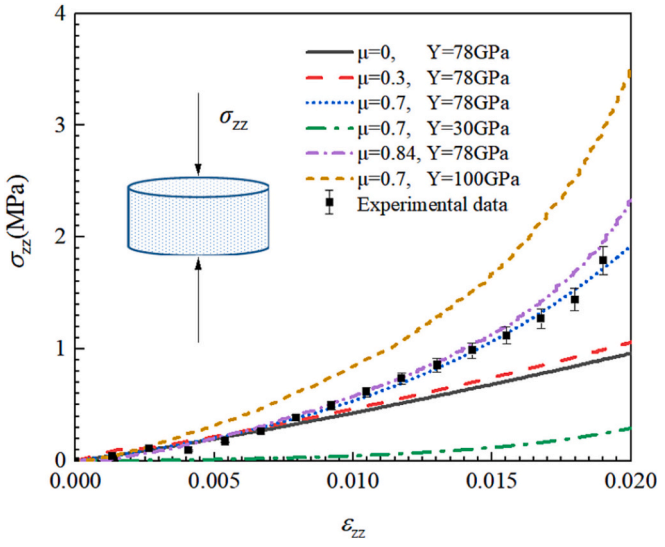

Fig. 2. Stress vs. strain obtained in simulations from different combinations of (Y, m) and the experimentally measured curve.

The interactions between the explosive elements and the particles in contact are accounted for by a normal linear spring with a normal stiffness $k_{n,p\text{-}e}$. If there is more than one particle in contact with one edge/surface of an explosive element, then the summation of the normal forces arising from all particles will be interpolated to the edge/surface nodes. Normally, the size of the explosive elements in contact with particles should be larger than the particle size. Otherwise, the outermost layer of fine explosive elements experiences nonuniform particle confinement during the violent expansion of gaseous detonation products. Severe distortion of explosive meshes likely ensues, leading to numerical divergence. However, explosive elements much larger than the particles can cause artificial directional stress transmission in particles since particles in contact with one explosive element edge/surface are subjected to forces in the same direction. We perform a convergence study of the ratio between the explosive element size and the particle diameter in contact with an element edge/surface and found that convergence is reached when the ratio ranged from 3 to 10.

As reported in previous studies, air diffusion through interparticle pores and the associated gaseous pressure rise are trivial during dynamic pressure wave propagation in the particle skeleton. Additionally, the presence of air outside the sand ring/shell has little effect on the impulse carried by the sand ejecta. Therefore, the interstitial and surrounding air is not taken into account in this work.

3. Problem formation and numerical setup

Buried blasts, especially shallow buried blasts, are often investigated using a stratified configuration wherein the central explosive is enclosed by a cylindrical (2D) or spherical sand shell (3D), as shown in Fig. 3 (a) and (b), respectively. By varying the sand shell thickness, the influence of the depth of burial (DOB) on a variety of resultant phenomena, such as the blast loading on nearby targets, throw-out distance of the sand ejecta, and mitigation of the blast wave, can be studied. In addition, in the rotational symmetric configuration, the divergent spherical compression wave through the sand shell is normal to the sand–air surface, only converting to a convergent tensile wave upon reflection, and no shear wave is present. Therefore, we also utilize the charge-sand stratified cylindrical and spherical configuration to investigate the buried blast-induced dynamic pressure waves.

As illustrated in Fig. 3 (a) and (b), the particle ring/shell domain, with inner and outer radii of $R_{in,0}$ and $R_{out,0}$, is filled by polydisperse discs/spheres generated by the radius expansion algorithm. Insets in (a) and (b) show the local packing structures wherein the particles are colored according to the local volume fraction defined as the disk area or sphere volume divided by the area or volume of its Voronoi cell. A population of particles, with artificially small radii that ensure no particle overlap, is randomly created within the specified domain. Then, all particles are expanded until the specified parcel size distribution and desired packing fraction, f_0, are both satisfied. After each incremental expansion, we examine the overlap between adjacent particles. For the pairs with an overlap, we either assign random small displacements to them or shrink their diameters to eliminate the overlap. The cumulative distribution curve of particle diameters, d_p, is presented in Fig. 3 (c), yielding a mean value of 550 mm. The zoomed-in images in the insets of Fig. 3(a) and (b) demonstrate the random packing of particles in the

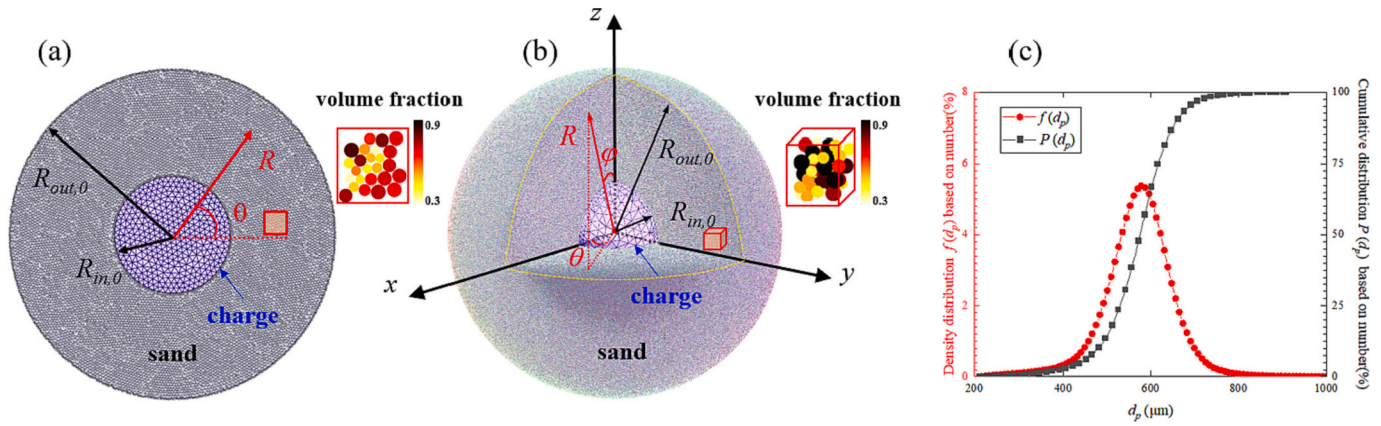

Fig. 3. Computational geometries of 2D cylindrical (a) and 3D spherical (b) configurations showing the central charge and surrounding particle ring/shell domains. (c) The Gaussian distribution of the particle diameter, $f(d_p)$, and the corresponding cumulative distribution, $P(d_p)$.

particle ring/shell without discernable crystallization. To better depict the statistical behaviors of stochastic particle assemblies, more than five realizations with the same particle size distribution and volume fraction are established for each numerical test to assess the variabilities among different realizations. For clarity, the system is labeled with four symbols, C or S-$R_{in,0}$ (unit mm) – $R_{out,0}$ (unit mm)-f_0, where C and S denote 2D cylindrical and 3D spherical configurations, respectively. The charge type, the material density of the particle and the particle size distribution are kept consistent among all numerical systems. The effects of various structural parameters with respect to the momentum transfer between the charge and the surrounding sand can be properly incorporated into one dimensionless parameter, namely, the mass ratio between the surrounding particles and the charge, M/C, the inverse of which indicates the imparted energy per unit mass of enclosing materials.

$$M\Big/C=\begin{cases}\dfrac{\rho_p\phi_0\left(R_{out,0}^2-R_{in,0}^2\right)}{\rho_{\exp}R_{in,0}^2} & \text{for a cylindrical configuration}\\[2ex] \dfrac{\rho_p\phi_0\left(R_{out,0}^3-R_{in,0}^3\right)}{\rho_{\exp}R_{in,0}^3} & \text{for a spherical configuration}\end{cases} \tag{1}$$

In Eq. (1), r_p and $r_{\exp}$ are the particle material density and explosive density, respectively.

In total, 23 numerical systems are established, including six 3D spherical configurations and 17 2D cylindrical configurations, with M/C ranging from O(10^0) to O(10^2). Fig. 4 indicates the distribution of the numerical systems in the parameter space of {$R_{out,0}$, f_0, M/C}. Different colors and shapes of symbols are used to distinguish systems with different charge radii and belonging to different configurations. Specifically, two sets of systems, C-12-X-0.84 and S-12-X-0.68, are intended to investigate the thickness (equivalently DOB) effect, while the other two sets of systems, C-12-50-X and C-48-150-X, are intended to investigate the volume fraction effect. Since the volume fractions of the random close 2D and 3D packing composed of particles with the diameter range studied here are 0.84 and 0.68, respectively, systems C-12-X-0.84 and S-12-X-0.68 enable us to assess the difference between the 2D cylindrical and 3D spherical configurations. Systems with the same f_0 value but different $R_{in,0}$ values (12 mm vs. 48 mm) allow for the investigation of the charge size.

4. Validation of the simulations

Buried blast simulations, especially shallow buried blasts, are often validated against blast loading experimental measurements of nearby structures. Equivalently, the prediction accuracy of the momentum

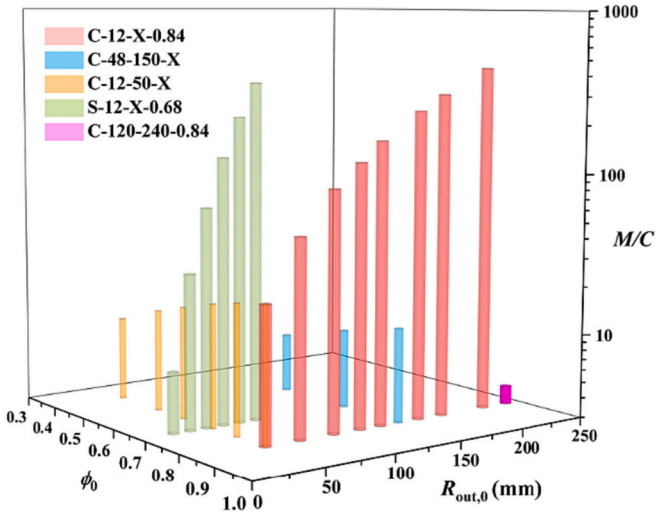

Fig. 4. Distribution of the structural parameters, $R_{out,0}$, f_0, and M/C and the charge configuration for systems that are to be numerically investigated. C-12-X-0.84: M/C range from 21 to 436, C-48-150-X: M/C range from 7 to 11.6, C-12-50-X: M/C range from 10 to 21, S-12-X-0.68: M/C range from 7 to 363, C-120-240-0.84: M/C is 4.

carried by the sand ejecta measures the reliability of the shallow buried blast simulation. For cylindrical or spherical charge-sand stratified configurations, both experiments and the resolved DEM simulations have found that the velocity predicted by the modified Gurney Eq. [35], $V_{G,f}$, provides a reliable estimation for the particle shell expansion velocity, i.e., the initial velocity of the sand ejecta [36]. Therefore, in this section, we justify our simulations by comparing the simulated expansion velocity of the sand ring/shell with theoretical predictions. $V_{G,f}$ is a function of the Gurney energy, E_G, the mass ratio, M/C, the solid phase volume fraction, f_0, and the particle material density, r_p.

$$\begin{aligned} V_{G,\phi}&=\sqrt{2E_G}\left(\frac{M/C}{\alpha(\rho_p)}+\frac{n}{n+2}\right)^{-0.5}\cdot F(\phi_0,M/C)\\ \alpha(\rho_p)&=a_0\rho_p^{a_1}\\ F(\phi_0,M/C)&=1+[a_2exp(a_3\phi_0)-0.5]lg\left(\frac{M}{C}\right)\end{aligned} \tag{2}$$

where constants $n=2$, $a_0=0.2$, $a_1=0.18$, $a_2=0.162$ and $a_3=1.127$ for the cylindrical configuration, and $n=3$, $a_0=0.2$, $a_1=0.18$, $a_2=0.162$ and $a_3=1.127$ for the spherical configuration.

The charge used in this paper is 2,4,6-trinitrotoluene (TNT), of which the density, internal energy and detonation velocity are taken from the optimized TNT JWL-EOS parameters in B Mobaraki et al. [37]. The JWL-EOS expresses the pressure as a function of relative volume and internal energy according to

$$p = A\left(1-\frac{\omega}{R_1 V}\right)exp(-R_1 V)+B\left(1-\frac{\omega}{R_2 V}\right)exp(-R_2 V)+\omega E \tag{3}$$

where A, B, R_1, R_2 and w are constants, $V = r/r_{\exp}$ is the ratio of the current and initial densities and E is the internal energy. The JWL-EOS parameters for the TNT charge are listed in Table 1. The Gurney energy of TNT is $E_G = 2.8$ MJ/kg. The sand particle parameters are set as in the quasistatic uniaxial compression test.

Fig. 5(a) shows the time histories of the mean velocity of sand rings/shells in typical systems scaled by $V_{G,f}$, $\widetilde{V}_{mean} = V_{\text{mean}}/V_{G,f}$. After the initial acceleration phase, $\widetilde{V}_{mean}$ begins to converge due to the drastic drop in pressure in the denotation products. Different damping coefficients, x, lead to different acceleration histories of V_{mean} and converged V_{mean} since x dictates the energy dissipation due to the inelastic interparticle collisions. Properly increasing x can incorporate the energy loss arising from the escape of the denotation products, which is absent in the FEM-DEM simulations. Fig. 5(b) presents the ratio of the converged mean velocity and the predicted expansion velocity, $V_{\text{mean,con}}/V_{G,f}$, using different values of x. Clearly, $x = 0.2$ gives rise to the ratio closest to unity. Hence, x is set to 0.2 in the present simulations. The dependences of $V_{\text{mean,con}}$ on the M/C in the 2D cylindrical and 3D spherical configurations shown in Fig. 5(c) using $x = 0.2$ are consistent with those predicted by Eq. (2).

According to the modified Gurney equation (Eq. (2)), for systems with the same M/C and f_0, the Gurney velocity and the resulting characteristic time scale with the square root of the Gurney energy is

$$\frac{V_G^m}{V_G^n} = \frac{t_n}{t_m} = \sqrt{\frac{E_G^m}{E_G^n}} \tag{4}$$

where the subscripts m and n represent systems m and n with Gurney energies E_G^m and E_G^n, respectively. Mo et al. [28] utilized resolved DEM simulations of the explosive dispersal of sand shells as a function of E_G. Using the velocity and time scaling law given in Eq. (4), we plot the scaled V_G vs. scaled t curves from the present FEM-DEM simulations against the curves derived from the resolved DEM, as shown in Fig. 6 (a)-(c). Here, the time t and the mean expansion velocity V_{mean} are scaled to $t\sqrt{E_G/E_G^{Mo}}$ and $V_{\text{mean}}\sqrt{E_G^{Mo}/E_G}$, respectively, where E_G^{Mo} is the Gurney energy used in the resolved DEM simulations, E_G^{Mo}=5 MJ/kg. The good agreement among the scaled expansion velocities in time space derived from the resolved and unresolved DEM simulations indicates that the unresolved DEM can produce comparable dynamic responses of particles subjected to blast loading if proper parameters are used.

5. Results

5.1. Wave system

To understand the flow patterns associated with the enclosed explosion, the space-time (R-t) diagrams of the pressure fields in different systems are constructed using the circumferentially averaged pressure, $\langle P\rangle$, as displayed in Fig. 7 (a)-(f). The pressure inside the gas pocket enclosed by the inner surface of the particle ring is the gaseous pressure of the detonation products, while the pressure in the particle ring domain represents the pressure sustained in the particle skeleton. The calculation of the particle phase pressure from the contact forces on the particles is presented in Appendix I. Despite the differences in the ring geometry and the initial volume fraction, a consistent basic flow pattern emerges as a result of the complex wave system. Based on the R-t diagram of the pressure field in system C-48-150-0.69 (see Fig. 7(b)), we plot the $\widetilde{r}$-$\widetilde{t}$ diagram of various waves in Fig. 8(a), showing the trajectories of the waves present in the detonation products and the particle ring as well. Here, the spatial coordinate is scaled by the thickness of the ring, $\widetilde{r} = (R - R_{\text{in},0})/(R_{\text{out},0} - R_{\text{in},0})$. The time is scaled by a timescale based on the velocity of the DW and the ring thickness, $\widetilde{t} = t/t$,

$$\tau = \left(R_{out,0} - R_{in,0}\right)\Big/\left(M_{exp}\sqrt{\frac{P_{CJ}}{\rho_{exp}}}\right) \tag{5}$$

For the charge made of TNT, the Mach number of the DW is $M_{\exp} = 3.22$, leading to $t = 3.28$ μs and 8.82 μs for particle rings with thicknesses of 38 mm and 102 mm, respectively.

As illustrated in Fig. 8(a), the detonation at the charge center issues an outgoing detonation wave (DW) and a tailing Riemann expansion wave with a head (REW_h) moving outward and a tail (REW_t) immediately following the DW. As the DW impinges the inner surface of the particle ring at $\widetilde{t}_{\text{DW,in}}$, a reflect shock wave (RSW) is set up while a transmitted blast wave (BW) traverses the particle ring, compacting the particles in its wake. Alongside the DW, the REW_t is transmitted into particles, converting into the head of the transmitted expansion wave (TEW_h). The blast-compacted particles are immediately unloaded. Thereafter, the REW_h interacts with the particle ring at $\widetilde{t}_{\text{REW}_\text{h},\text{in}}$, evolving into the tail of the transmitted expansion wave (TEW_t) after having reflected off the inner surface as $\text{REW}_\text{t}^{\text{inward}}$. Finally, the BW reflects off the outer surface of the ring at $\widetilde{t}_{\text{BW,out}}$ and transitions into an inward-going rarefaction wave (RW). The RW fully releases the particle phase pressure and accelerates the compacted particles. As RW reflects off the inner surface at $\widetilde{t}_{\text{SSW,in}}$, a secondary shock wave (SSW) emanates from the inner surface, recompacting particles in its wake. Notably, the strength of the SSW is at least one order of magnitude smaller than that of the BW in terms of the immediate pressure jump (see Fig. 7). As a result of the interaction with complex waves, the expansion of the inner surface sets in at $\widetilde{t}_{\text{DW,in}}$ and exhibits two kinks upon the arrival of the REW_h and the commencement of the SSW at $\widetilde{t}_{\text{REW}_\text{h},\text{in}}$ and $\widetilde{t}_{\text{SSW,in}}$, respectively. The scaled displacement of the inner surface at $\widetilde{t}_{\text{REW}_\text{h},\text{in}}$ is $\widetilde{R}_{\text{in,REW}_\text{h}}$. The outer surface accelerates upon the BW reflecting off the outer surface at $\widetilde{t}_{\text{BW,out}}$. With the expansion of the inner surface, the overall pressure in the denotation products substantially decreases, smoothing out the pressure gradients across various waves (see Fig. 7). Actually, the trajectories of the outward reflected shock wave ($\text{RSW}^{\text{outward}}$) and reflected expansion wave ($\text{REW}^{\text{outward}}$) from the charge center are barely discernable. Fig. 8(b) plots the $\widetilde{r}$-$\widetilde{t}$ diagrams of the BW, TEW_t and RW in typical systems with varying f_0 and $R_{\text{in},0}$, displaying nontrivial variations in the wave dynamics.

Fig. 9 (a) and (b) plot the trajectories of the BW and the TEW_t in densely packed cylindrical (systems C-12-X-0.84) and spherical (systems S-12-X-0.68) particle shells with varying thicknesses, respectively. The slowing down of the BW becomes increasingly significant as the BW expands outward, which is more marked in the spherical systems. The slowing down of the BW accompanies the weakening of the strength, which is accounted for in Sec. 5.2. Table 2 lists the average velocities of the BW, TEW_t and RW, $\widetilde{\overline{V}}_{\text{BW}}$, $\widetilde{\overline{V}}_{\text{TEW}_\text{t}}$, $\widetilde{\overline{V}}_{\text{RW}}$, and the characteristic times, $\widetilde{t}_{\text{DW}}$, $\widetilde{t}_{\text{BW}}$, $\widetilde{t}_{REW_h}$ and $\widetilde{t}_{\text{SSW}}$, in all numerical systems. Here, $\widetilde{\overline{V}}_{\text{BW}}$, $\widetilde{\overline{V}}_{\text{TEW}_\text{t}}$ and $\widetilde{\overline{V}}_{\text{RW}}$ are dimensionless velocities scaled by the characteristic velocity, V

Table 1
Material model and EOS parameters of TNT.

$r_{\exp}$ (kg/m^3)	D (m/s)	P_{CJ} (GPa)	A (GPa)	B (GPa)	R_1	R_2	w	E (GPa)
1630	6930	21	373.8	3.747	4.15	0.9	0.35	6

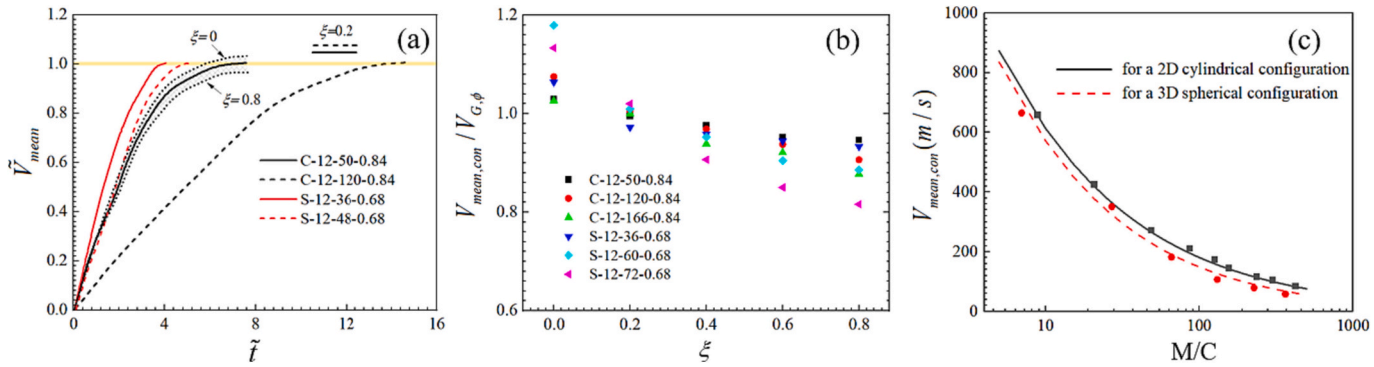

Fig. 5. Time histories of the mean velocity of sand rings/shells in typical systems (a), the ratio of the converged mean velocity and the predicted expansion velocity (b), and $V_{mean,con}$ on the M/C in 2D cylindrical and 3D spherical configurations (c).

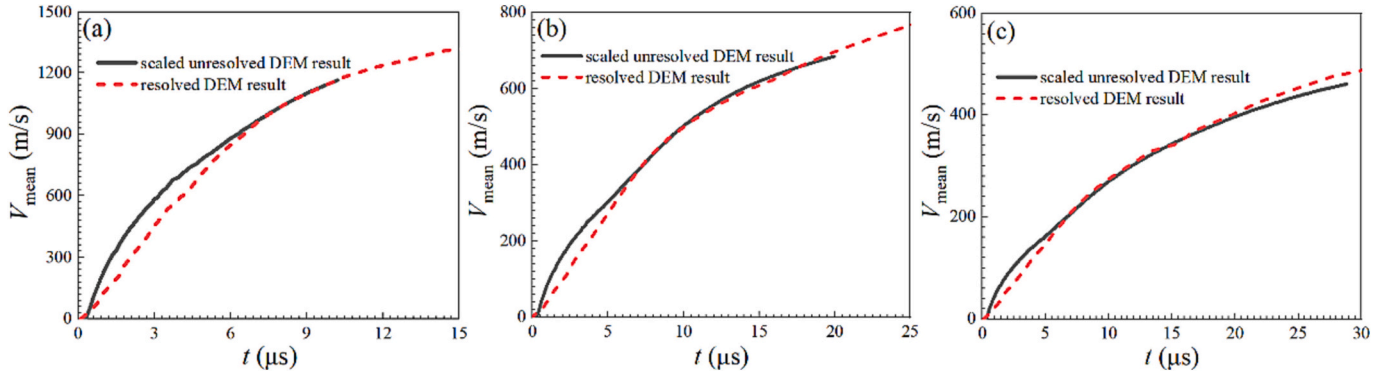

Fig. 6. The scaled V_G vs. scaled t curves from the present FEM-DEM simulations against the curves derived from the resolved DEM simulations: (a) the M/C is approximately 4.7, (b) the M/C is approximately 13, and (c) the M/C is approximately 27.

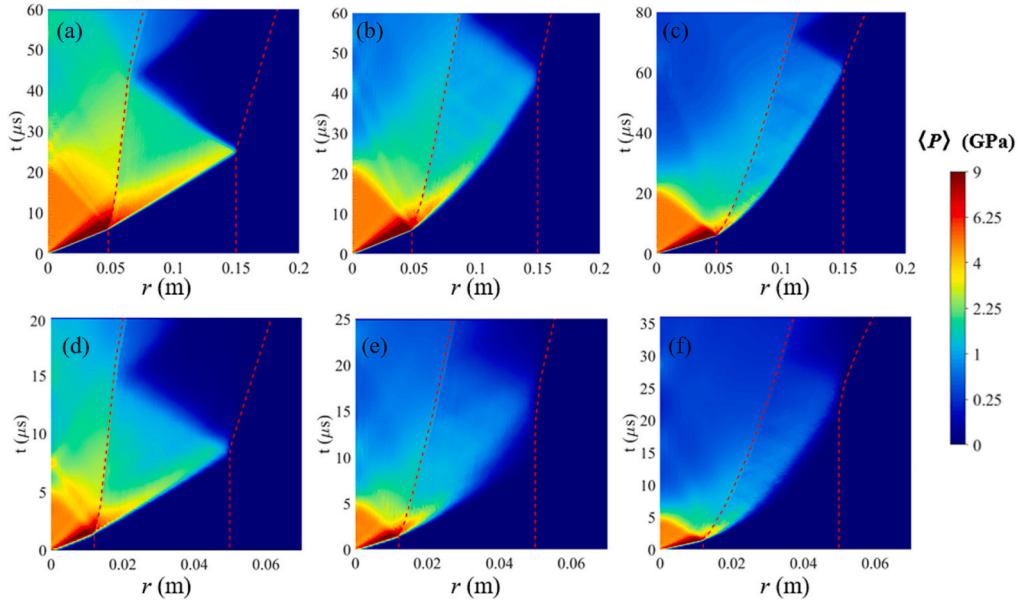

Fig. 7. Space-time (R-t) diagrams of the pressure fields in systems C-48-150-0.84 (a), C-48-150-0.69 (b), C-48-150-0.52 (c), and C-12-50-0.84 (d), C-12-50-0.69 (e),C-12-50-0.52 (f). Dashed lines represent the trajectories of the inner and outer surfaces of the particle rings.

$= (R_{out,0}\text{-}R_{in,0})/t = M_{exp}^{-1}\sqrt{\rho_{exp}/P_{CJ}}$, $\widetilde{\overline{V}}_{BW} = \overline{V}_{BW}/\varsigma$, $\widetilde{\overline{V}}_{TEW_t} = \overline{V}_{TEW_t}/\varsigma$, $\widetilde{\overline{V}}_{RW} = \overline{V}_{RW}/\varsigma$. The slowing down of the BW results in a decrease in $\widetilde{\overline{V}}_{BW}$ with increased ring thickness and with decreased initial volume fraction. In 2D cylindrical configurations, as the M/C increases from 21 to 436 for small radius (R_{in} = 12 mm) charges, the $\widetilde{\overline{V}}_{BW}$ decreases by 22.2%. Similarly, in 3D spherical configurations, as the M/C increases from 7 to 363, the $\widetilde{\overline{V}}_{BW}$ decreases by 15.4%. Moreover, for 2D cylindrical configurations with small radius (R_{in} = 12 mm) and large radius (R_{in} = 48 mm)

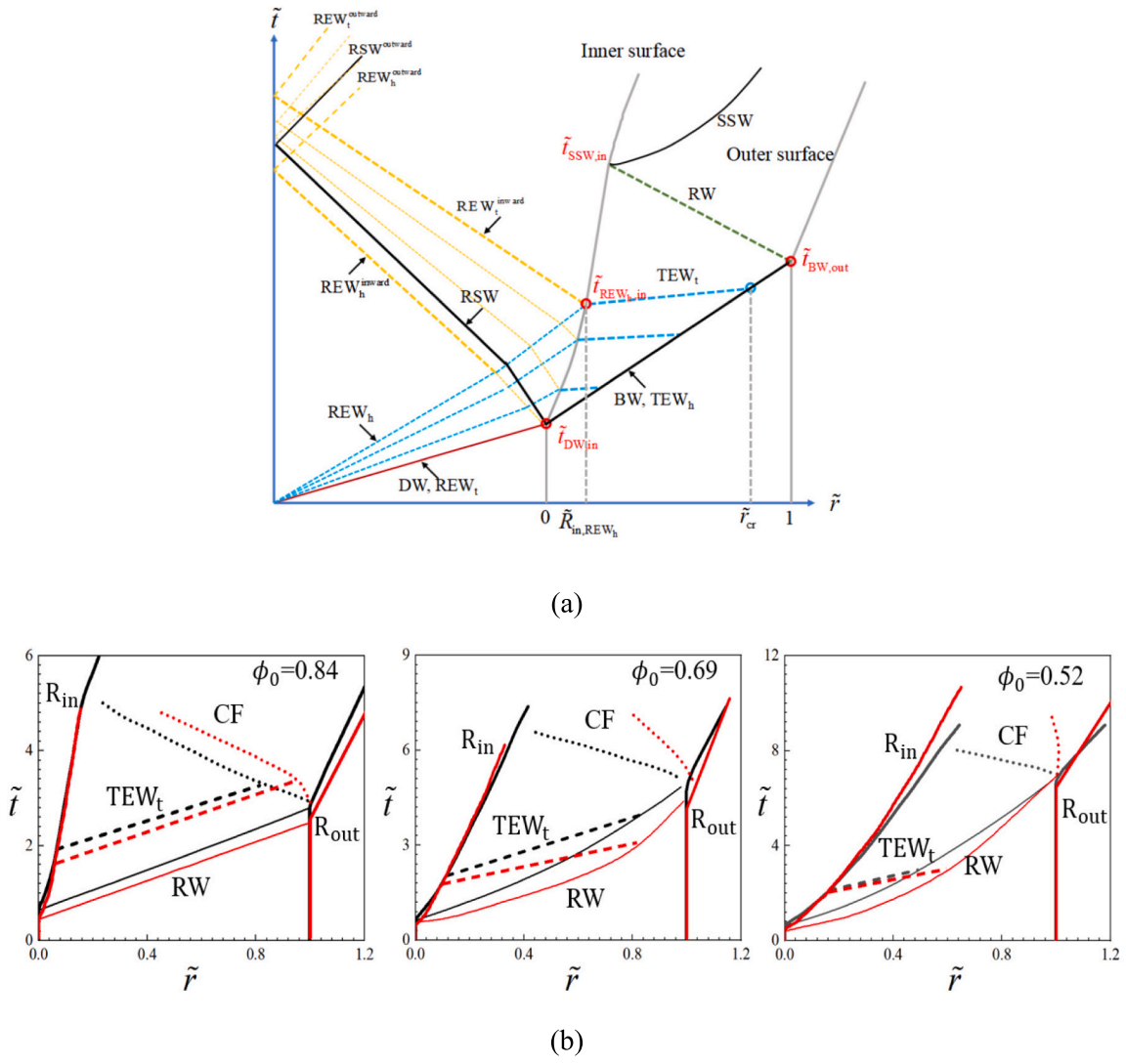

Fig. 8. (a) $\tilde{r}$-$\tilde{t}$ diagram showing the propagation of various waves. (b) Comparison of the propagation of the BW, TEW_t and RW in systems C-48-150-0.52, C-48-150-0.69, C-48-150-0.84, C-12-50-0.52, C-12-50-0.69, and C-12-50-0.84. The black line is C-48-150-X , and the red line is C-12-50-X.

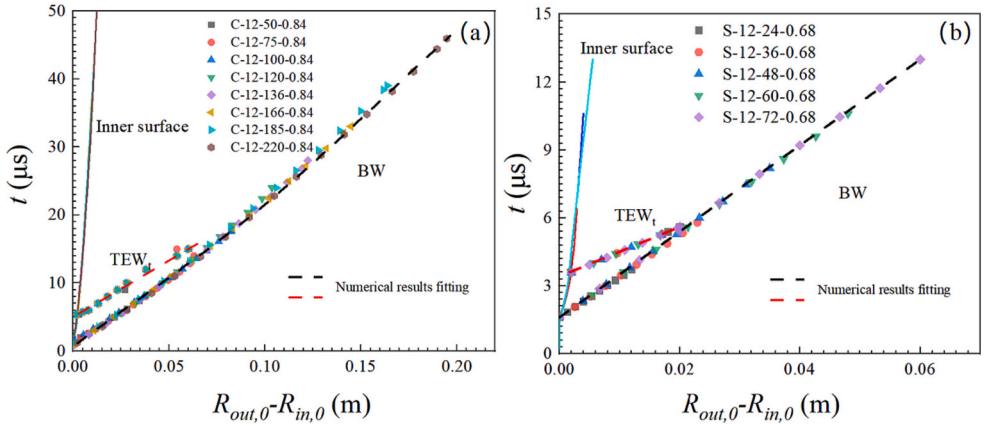

Fig. 9. Trajectories of the BW and TEW_t in densely packed cylindrical (systems C-12-X-0.84) (a) and spherical (systems S-12-X-0.68) (b) particle shells. The dashed lines represent the fitting lines of the trajectories of the BW and TEW_t in particle shells with increasing thickness.

charges, as the initial volume fraction decreases from 0.84 to 0.52, the $\widetilde{\overline{V}}_{BW}$ decreases by 42.6% and 39.1%, respectively. A stronger correlation between $\widetilde{\overline{V}}_{BW}$ and $\widetilde{\overline{V}}_{RW}$ is discernable. A stronger, faster BW upon reflection off the outer surface transitions into a faster RW. Otherwise, a weak RW decays quickly while traveling inward so that it cannot reach the inner surface of the ring, leading to an infinite $\widetilde{\overline{V}}_{RW}$,

Table 2
Parameters pertinent to the propagations of various waves.

ID	$\widetilde{\widetilde{V}}_{BW}$	$\widetilde{\widetilde{V}}_{TEW_t}$	$\widetilde{\widetilde{V}}_{RW}$	$\widetilde{t}_{DW,in}$	$\widetilde{t}_{BW,out}$	$\widetilde{t}_{SSW,in}$	$\widetilde{t}_{REW_{h,in}}$	$\widetilde{r}_{cr}$	$\widetilde{r}_{in,REW_h}$	$\widetilde{\widetilde{R}}^{I}_{out,th}$	$\widetilde{\widetilde{R}}^{II}_{out,th}$
C-12-50-0.84	0.472	0.52	0.446	0.49	2.62	4.63	1.46		0.053	2.7	
C-12-75-0.84	0.451	0.52	0.446	0.29	2.57	4.88	0.88	0.89	0.032		5.5
C-12-100-0.84	0.446	0.52	0.446	0.21	2.58	4.71	0.63	0.64	0.023		5.5
C-12-120-0.84	0.408	0.52	0.446	0.17	2.75	4.93	0.51	0.52	0.019		5.5
C-12-136-0.84	0.404	0.52	0.446	0.15	2.69	4.86	0.45	0.45	0.016		5.5
C-12-166-0.84	0.388	0.52	0.446	0.12	2.78	5.15	0.36	0.36	0.013		5.5
C-12-185-0.84	0.374	0.52	0.446	0.11	2.83	5.57	0.32	0.32	0.012		5.5
C-12-220-0.84	0.367	0.52	0.446	0.09	2.85	5.87	0.27	0.27	0.010		5.5
C-12-50-0.76	0.375	0.50	0.441	0.49	3.05	5.43	1.46	0.74	0.079		3.5
C-12-50-0.69	0.323	0.47	0.420	0.49	4.63	7.38	1.52	0.63	0.079		3.0
C-12-50-0.6	0.277	0.39	0.400	0.49	6.28	8.78	1.77	0.53	0.105		2.6
C-12-50-0.52	0.271	0.30	0.350	0.49	7.13	9.82	1.95	0.47	0.158		2.5
C-12-50-0.4	0.267	0.26	0.300	0.49	7.93	10.37	2.20	0.45	0.211		2.3
C-48-150-0.84	0.465	0.53	0.444	0.66	2.84	5.00	2.09		0.069	1.28	
C-48-150-0.69	0.319	0.46	0.413	0.66	4.91	7.04	2.27	1.31	0.137		2.8
C-48-150-0.52	0.283	0.31	0.382	0.66	6.95	8.29	2.73	0.96	0.216		2.1
C-120-240-0.84	0.472		0.462	1.29	3.17	4.91	4.91		0.2	1	
S-12-24-0.68	0.518	0.86	0.462	1.54	3.28	5.60	3.57	3.33	0.167	1.38	
S-12-36-0.68	0.485	0.86	0.462	0.77	2.90	4.92	1.79	1.67	0.083	2.13	
S-12-48-0.68	0.467	0.86	0.462	0.51	2.57	4.57	1.19	1.11	0.056		3.5
S-12-60-0.68	0.460	0.86	0.462	0.39	2.56	4.49	0.89	0.83	0.042		3.5
S-12-72-0.68	0.454	0.86	0.462	0.31	2.51	4.33	0.71	0.67	0.033		3.5
S-12-84-0.68	0.438	0.86	0.462	0.26	2.45	4.15	0.60	0.56	0.028		3.5

which is the case in systems C-12-50-0.4, C-12-50-0.52, and C-12-50-0.6. Since the TEW_t moves faster than the BW, the tailing TEW_t eventually catches up with the BW as long as the thickness of the ring is sufficiently large. Table 2 also presents the scaled distance from the inner surface of the ring upon which the TEW_t catches up with the BW, $\widetilde{r}_{cr}$. Notably, $\widetilde{\widetilde{V}}_{TEW_t}$ and $\widetilde{\widetilde{V}}_{RW}$ represent the absolute velocities of the TEW_t and RW rather than the relative velocities with regard to the local particles.

A close inspection the *R-t* diagrams of the pressure fields in different systems (Fig. 7(a)-(f)) shows that the initial volume fraction, f_0, and the inner radius of the particle ring, $R_{in,0}$, both play a significant role in the propagation of various waves. As shown in Fig. 8(b), the BW and the trailing TEW_t propagate much slower and attenuate much faster in the particle rings with smaller f_0. Likewise, the weakening of the BW becomes more significant in the particle rings with smaller $R_{in,0}$. Therefore, we observe the slowest BW in system C-12-50-0.4 with the smallest f_0 and $R_{in,0}$. These observations are substantiated by the $\widetilde{\widetilde{V}}_{BW}$ in these systems, as listed in Table 2.

5.2. Granular dynamics

The granular dynamics of the particle ring are governed by the waves present in the particles, including the BW, TEW_t, RW and SSW. Fig. 10 (a)-(f) depict the profiles of the circumferentially averaged particle phase pressure, $\langle P \rangle$, particle velocity, $\langle u_p \rangle$, and local volume fraction, $\left\langle \phi_p \right\rangle$ in the systems with varying f_0, namely, C-48-150-0.52, C-48-150-

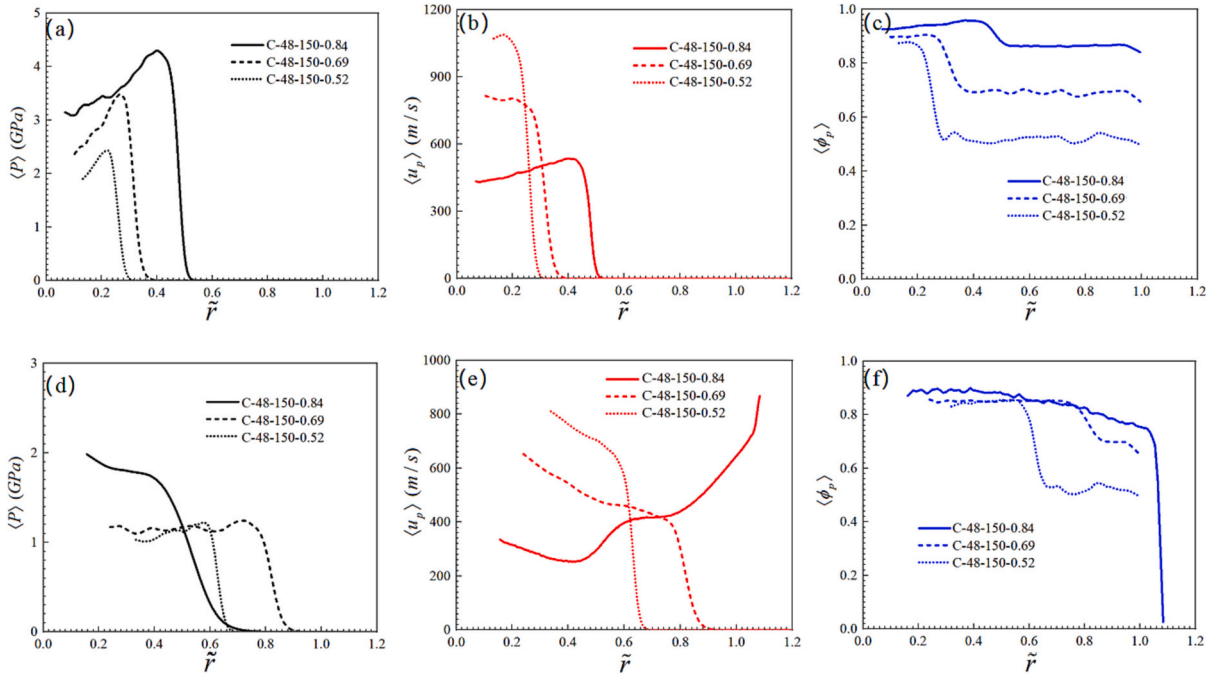

Fig. 10. Comparison of the profiles of $\langle P \rangle(\widetilde{r})$ (a, d), $\langle u_p \rangle(\widetilde{r})$(b, e) and $\left\langle \phi_p \right\rangle(\widetilde{r})$(c, f) in systems with varying f_0 at times $\widetilde{t} = 1.7$ (*a*, *b*, *c*) and 3.98 (d, e, f).

0.69, and C-48-150-0.84, at $\tilde{t} = 1.7$ ($t = 15$ ms) and 3.98 ($t = 35$ ms). Accordingly, the arrival of the BW results in a sharp jump in the profiles of $\langle P\rangle(\tilde{r})$, $\langle u_p\rangle(\tilde{r})$ and $\langle \phi_p \rangle(\tilde{r})$ (see Fig. 10(a)-(c), respectively). The tailing TEW is responsible for the immediate drop in $\langle P\rangle$, forming a prominent pressure peak. As seen in Fig. 10(a), the peak pressure, $\langle P_{\text{peak}}\rangle$, and the pressure peak amplitude both decrease with f_0, indicating the weakening of the TRW_t and the BW with smaller f_0. In contrast, the $\langle u_p\rangle$ of blast-compacted particles increases with decreasing f_0 (see Fig. 10(b)). At $\tilde{t} = 3.98$ ($t = 35$ ms), the TRW_t has caught up with the BW in systems C-48-150-0.52 and C-48-150-0.69. Hence, the sudden jumps in the $\langle P\rangle(\tilde{r})$ profiles are followed by a plateau (see Fig. 10(d). At the same time, the particle ring in system C-48-150-0.84 is swept by the inward-going RW. As a result, $\langle P\rangle$ and $\langle \phi_p \rangle$ dramatically decrease in the wake of the RW, while the part of the $\langle u_p\rangle$ profile affected by the RW is lifted up.

The effect of $R_{\text{in},0}$ on the granular dynamics is demonstrated in Fig. 11(a)-(c), which compares the profiles of $\langle P\rangle(\tilde{r})$, $\langle u_p\rangle(\tilde{r})$ and $\langle \phi_p \rangle(\tilde{r})$ in systems C-48-150-0.52 and C-12-50-0.52, C-48-150-0.69 and C-12-50-0.69, and C-48-150-0.84 and C-12-15-0.84, respectively. Similar to the influence of f_0, a smaller $R_{\text{in},0}$ leads to a lower $\langle P_{\text{peak}}\rangle$ and a reduced peak amplitude (see Fig. 11(a)). However, unlike f_0, the blast-compacted particles gain smaller velocities in the particle rings with smaller $R_{\text{in},0}$ (see Fig. 11(b)). In addition, the weakened BW in the systems with small $R_{\text{in},0}$ cannot compact the particles to the same volume fraction as systems with large $R_{\text{in},0}$, as indicated in Fig. 11(c).

The $\langle P\rangle(\tilde{r})$ profiles plotted in Fig. 10(a), (b) and Fig. 11(a) are derived from the quasistatic part of the total particle phase stresses, σ_{ij}^c, which is accounted for in most consolidation-type soil mechanics models [38–40]. Although the present interparticle contact model assumes that particles in contact undergo linear elastic deformation rather than the viscoplastic deformation in standard soil consolidation models, the explicit correlation between σ_{ij}^c and the volume fraction, $\langle \phi_p \rangle$, is consistent with the conventional continuum models. Thus, the decay law of $\langle P_{\text{peak}}\rangle$ and the influences of structural parameters revealed in this work are universal and shed fundamental light on the propagation of the BW in particle packings.

Fig. 12(a) displays the decay of $\langle P_{\text{peak}}\rangle$ with a scaled distance from the inner surface, $\langle P_{\text{peak}}\rangle(\tilde{r})$, in the systems investigated in Fig. 7(a)-(f). Except for systems C-12-50-0.84 and C-48-150-0.84, the $\langle P_{\text{peak}}\rangle(\tilde{r})$ curves in the other systems feature a rapid decline, followed by a tempered decline and a sudden drop in a narrow region adjacent to the outer surface of the ring. Although the geometric expansion and the interparticle dissipation both contribute to the attenuation of the BW, the primary physics underlying the decay of $\langle P_{\text{peak}}\rangle$ is related to the wave dynamics and the coupling between the ring and detonation

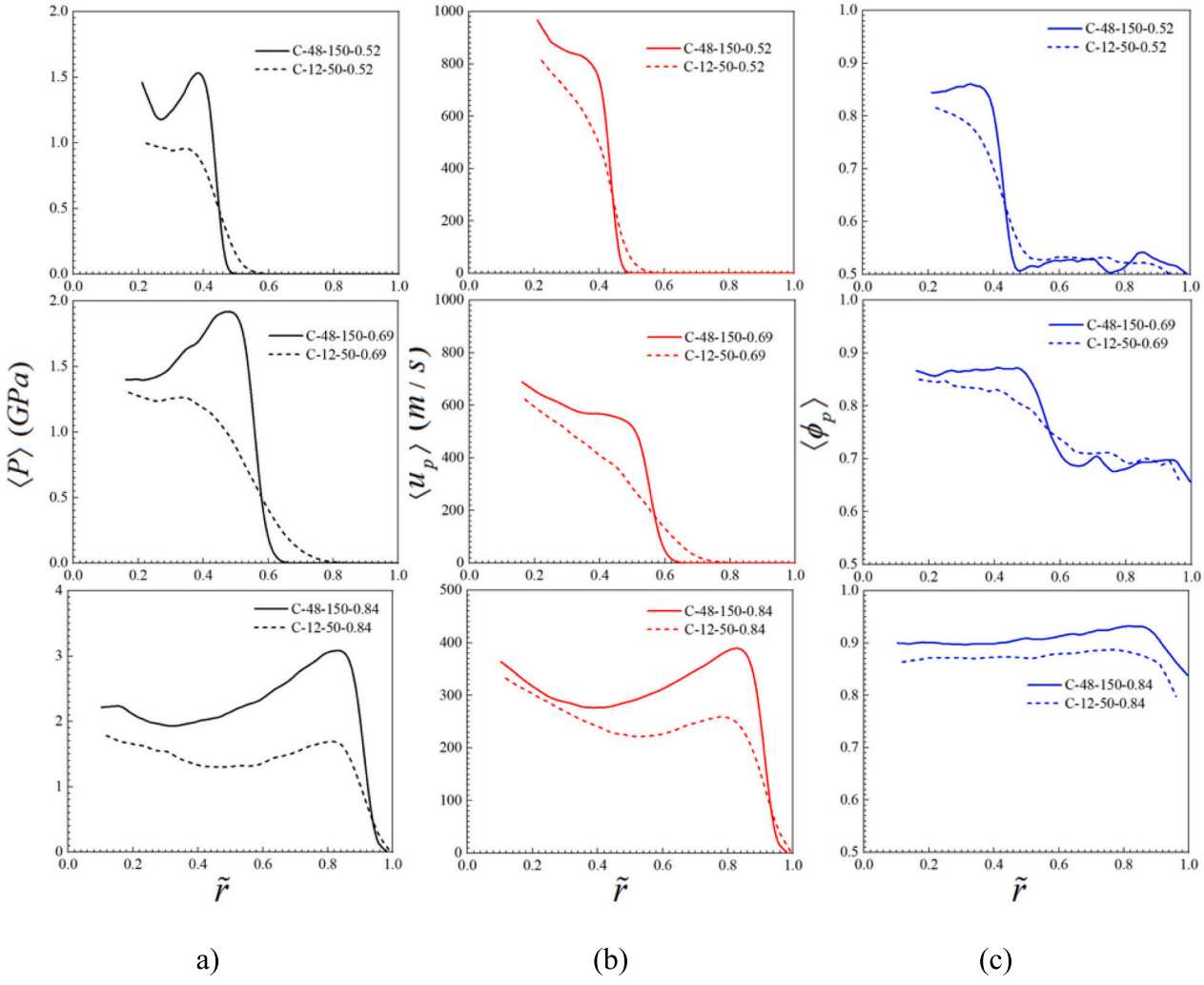

Fig. 11. Comparison of the profiles of $\langle P\rangle(\tilde{r})$ (a), $\langle u_p\rangle(\tilde{r})$(b) and $\langle \phi_p \rangle(\tilde{r})$(c) in systems with varying $R_{\text{in},0}$ at times $\tilde{t} = 2.6$. Top row: systems C-48-150-0.52 and C-12-50-0.52; middle row: systems C-48-150-0.69 and C-12-50-0.69; bottom row: systems C-48-150-0.84 and C-12-50-0.84.

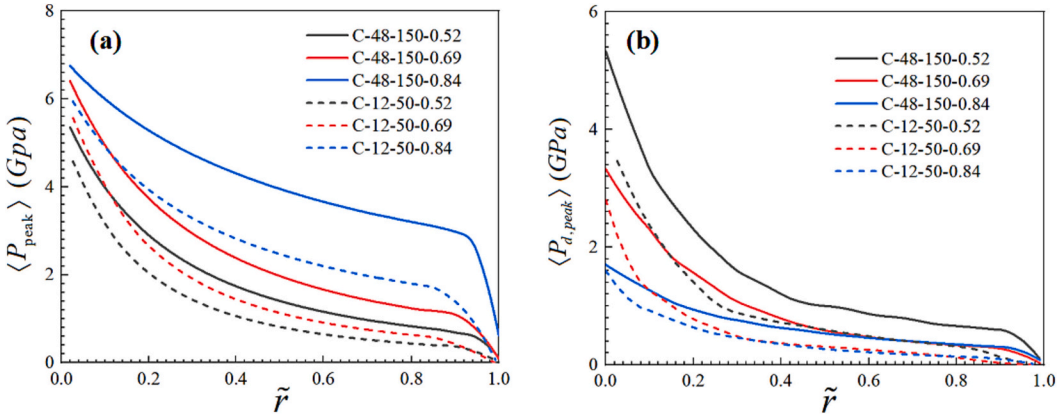

Fig. 12. Decay of the static and dynamic particle phase pressure peak with the scaled distance from the inner surface, $\langle P_{peak} \rangle(\tilde{r})$ (a) and $\langle P_{d,peak} \rangle(\tilde{r})$(b) in the systems investigated in Fig. 7(a)-(f).

products. As indicated in Fig. 8(a) and (b), the transmitted expansion fan with the head TEW_h and the tail TEW_t gradually coalescences with the preceding BW, giving rise to the rapid decline of the $\langle P_{peak} \rangle$ until the TEW_t catches up with the BW. Thereafter, the gradual decrease in the pressure in the central gas pocket due to the expansion of the detonation products is responsible for the tempered decline in $\langle P_{peak} \rangle$. The final sudden drop in the $\langle P_{peak} \rangle(\tilde{r})$ curve is associated with the dispersion of the BW since $\langle P_{peak} \rangle$ is averaged over the front width of the BW. The dispersion of the BW manifested by the widening of the divergent blast front is discussed below. In systems C-12-50-0.84 and C-48-150-0.84, the TEW_t does not catch up with the BW when the latter reaches the outer surface so that the rapid decline phase of $\langle P_{peak} \rangle$ is truncated by the sudden drop.

As shown in Fig. 12 (a), smaller values of f_0 and $R_{in,0}$ result in a faster decline in $\langle P_{peak} \rangle$. This can be understood by the coupling between the detonation products and the particle ring. Specifically, the acceleration of the expanding inner surface supplies additional expansion waves traveling upstream, albeit with weak intensity, further lowering gaseous pressure exerted on the inner surface, which is already being reduced by the impinging REW. Consequently, the transmitted expansion wave

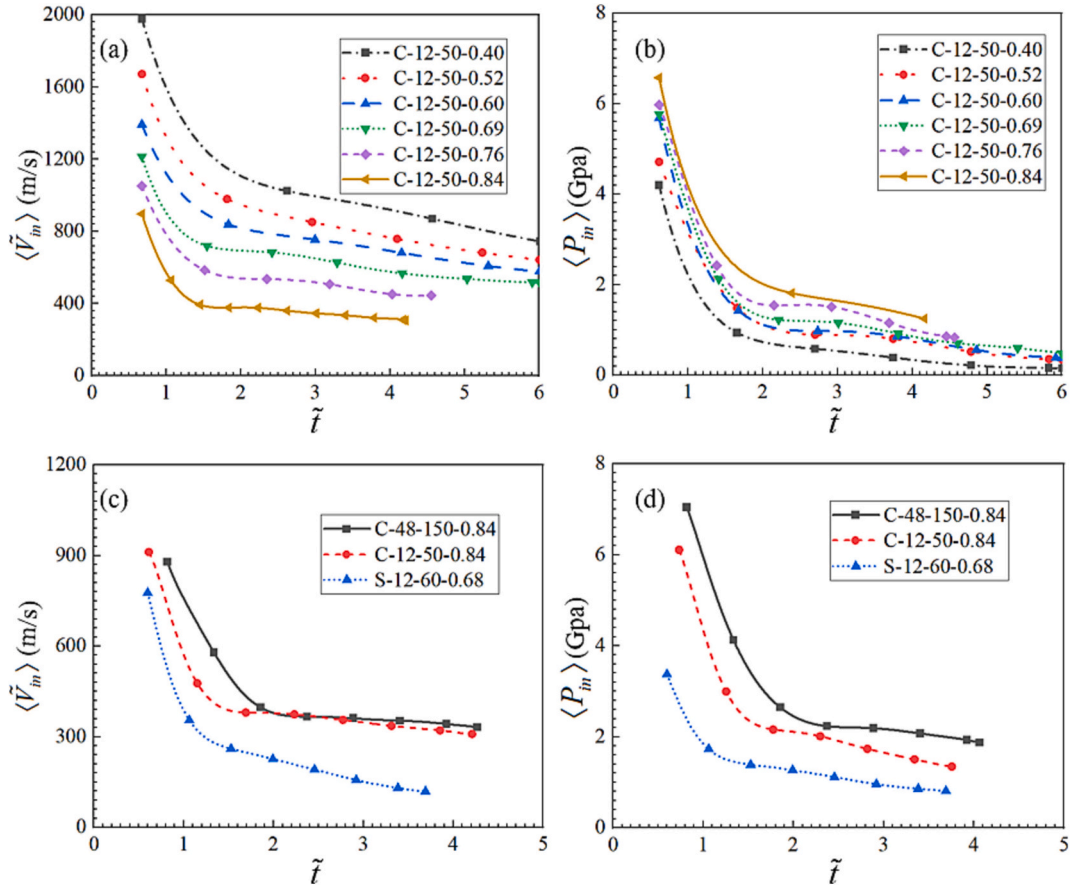

Fig. 13. Time histories of the innermost layer's velocity, $\left\langle \tilde{V}_{in} \right\rangle(\tilde{t})$ (a, c), and the gaseous pressure exerted on the inner surface, $\langle P_{in} \rangle(\tilde{t})$ (b, d), in systems with varying f_0 and $R_{in,0}$. (a), (b): systems C-12-50-X (X = 0.4, 0.52, 0.6, 0.69, 0.76, 0.84); and (c), (d): systems C-48-150-0.84, C-12-50-0.84 and S-12-60-0.68.

TEW is enhanced, attenuating the BW faster. Fig. 13(a) and (b) show the time histories of the innermost layer's velocity, $\left\langle \widetilde{V}_{\mathrm{in}} \right\rangle(\tilde{t})$, and the gaseous pressure exerted on the inner surface, $\langle P_{\mathrm{in}} \rangle(\tilde{t})$, respectively. Loose particle packings with lower f_0 show larger $\left\langle \widetilde{V}_{\mathrm{in}} \right\rangle$ and more rapidly declining $\langle P_{\mathrm{in}} \rangle$, whereby the decay of $\langle P_{\mathrm{peak}} \rangle$ becomes faster. The coupling between the detonation products and particle ring is more significant in systems with a smaller volume of the charge, namely, smaller $R_{\mathrm{in},0}$, as well as in a spherical configuration. As shown in Fig. 13 (c) and (d), the comparison of $\left\langle \widetilde{V}_{\mathrm{in}} \right\rangle(\tilde{t})$ and $\langle P_{\mathrm{in}} \rangle(\tilde{t})$ in systems C-48-150-0.84, C-12-50-0.84 and S-12-60-0.68 suggests that system S-12-60-0.68 has the largest $\left\langle \widetilde{V}_{\mathrm{in}} \right\rangle$ and fastest decay of $\langle P_{\mathrm{in}} \rangle$. Therefore, $\langle P_{\mathrm{peak}} \rangle$ decays faster in particle rings with smaller $R_{\mathrm{in},0}$ and in a spherical configuration as well.

Another important part of the total particle phase stress is related to the particle inertia, known as the dynamic stress, σ_{ij}^{d}, which constitutes the dynamic pressure, P_{d}. The deviation of P_{d} is presented in Appendix I. The $\langle u_p \rangle(\tilde{r})$ profiles shown in Fig. 10(b), (e) and Fig. 11(b) are indicative of the corresponding profiles of $\langle P_{\mathrm{d}} \rangle(\tilde{r})$. Similar to $\langle u_p \rangle(\tilde{r})$, the peak values of the dynamic pressure, $\langle P_{\mathrm{d,peak}} \rangle$, occur at the front of the BW. The decay of $\langle P_{\mathrm{d,peak}} \rangle$ with the propagation distance of the BW in various systems is plotted in Fig. 12(b), which exhibits a similar trend with its static counterpart. However, smaller f_0 and $R_{\mathrm{in},0}$ lead to slower decay of $\langle P_{\mathrm{d,peak}} \rangle$ opposed to the f_0 and $R_{\mathrm{in},0}$ dependences of $\langle P_{\mathrm{peak}} \rangle(\tilde{r})$. Note that in all systems, $\langle P_{\mathrm{d,peak}} \rangle$ is one order of magnitude smaller than $\langle P_{\mathrm{peak}} \rangle$. Hence, the total particle phase pressure is dominated by the quasistatic pressure.

The dispersion of the BW is another noteworthy characteristic intrinsic to BW propagation through particles, which causes the spreading out of the leading edge of the $\langle P \rangle(\tilde{r})$ profile, as shown in Fig. 14. The width of the sloping leading edge of $\langle P \rangle(\tilde{r})$, known as the blast front width, Dh, increases with propagation distance, especially in systems with smaller f_0 and $R_{\mathrm{in},0}$. The widening of the blast front is related to the evolution of the heterogeneous network of force chains, which carries most of the load in particle packings. Fig. 15 (a)-(d) show snapshots of parts of blast-loaded particle rings wherein particles are colored by their instantaneous quasistatic pressure, P_{p}, and the particles in contact with the contact force beyond a threshold are connected by lines. The networks of force chains visualized in Fig. 15 are constituted by heavily compressed particles that infiltrate the blast compacted particles. The strong force networks become spatially sparse and inhomogeneous as f_0 and $R_{\mathrm{in},0}$ decrease (compare Fig. 15 (a), (b) and (c)). In the transition region between the compacted and uncompacted particles, finger-like chains of particles protruding into the uncompacted particles give roughness to the blast front (see insets in Fig. 15), leading to a blast front with a finite width, Dh. Dh increases as the blast front becomes increasingly rougher while expanding geometrically. When the far end of the blast front approaches the outer surface, an RW immediately reflects inward and unloads the particle phase stresses (see Fig. 15 (d)). Therefore, the outermost layers of particles with a thickness of Dh_{L} are barely affected by the BW, with Dh_{L} being the blast front width as it reaches the outer surface. Consequently, the $\langle P_{\mathrm{peak}} \rangle$ in the outermost annular region delimited by the circles with radii of $R_{\mathrm{out},0}$ – Dh_{L} and $R_{\mathrm{out},0}$ undergoes a substantial drop.

5.3. Dynamic characteristics of the particle phase pressure

The particle phase stress known as the effective stress, s, is the parameter responsible for the deformation and strength of the granular medium subjected to blast loading and inevitably affected by unsteady wave propagation. Previous studies based on shock tube experiments have determined that the s curves feature an initial unsteady peak, followed by a dramatic decrease caused by the rarefaction wave that originates inside the granular medium. In this section, we establish the correlation between the s curves represented by the pressure histories, $\langle P \rangle(\tilde{t})$, and the various waves detailed in Section 5.1.

At $\tilde{r} \le \tilde{r}_{cr}$ (see Fig. 16(a)), the $\langle P \rangle(\tilde{t})$ curve displays distinctive imprints left by the various waves traversing the particle ring. The initial sharp pressure peak is attributed to the BW and the ensuing TEW. The arrival of the TEW$_{\mathrm{t}}$ coincides with the onset of the second gradual decreasing phase of the $\langle P \rangle(\tilde{t})$ curve. The final sudden drop of the $\langle P \rangle(\tilde{t})$ curve is caused by the inward traveling RW. At $\tilde{r} > \tilde{r}_{cr}$, the TEW$_{\mathrm{t}}$ has caught up with the BW, and the initial pressure peak diminishes, D$\tilde{t}_I = 0$. The three-phase $\langle P \rangle(\tilde{t})$ curve evolves into a two-phase curve, as indicated in Fig. 16(b).

For particle rings with outer radii smaller than a threshold, $R_{\mathrm{out,th}}^{\mathrm{II}}$, the inward traveling RW encounters the outgoing TEW$_{\mathrm{t}}$ at $\tilde{r}_{\mathrm{RW}}$, as occurs in systems C-48-150-0.84 and C-12-50-0.84 (see Fig. 8(b)). In this case, the $\langle P \rangle(\tilde{t})$ curve in the annular region beyond $\tilde{r}_{\mathrm{RW}}$ declines from $\langle P_{peak} \rangle$ to zero caused by the combination of the TRW and the RW without noticeable kinks, as shown in Fig. 16 (c). In the system with the threshold outer radius, $R_{\mathrm{out,th}}^{\mathrm{II}}$, the BW and TEW$_{\mathrm{t}}$ simultaneously arrive at the outer surface; equivalently $R_{\mathrm{out,th}}^{\mathrm{II}} = r_{\mathrm{cr}}$. $R_{\mathrm{out,th}}^{\mathrm{II}}$ can be readily extracted from systems with a $\tilde{r}_{\mathrm{cr}}$ less than unity. For systems with infinite $\tilde{r}_{\mathrm{cr}}$, such as those with the most densely packed particles, $R_{\mathrm{out,th}}^{\mathrm{II}}$ is determined by extrapolating the trajectories of the BW and TEW$_{\mathrm{t}}$ until they intersect with each other. Upon the intersection between the RW and TEW$_{\mathrm{t}}$, $\tilde{t} = \tilde{t}_{\mathrm{RW}}$, we have

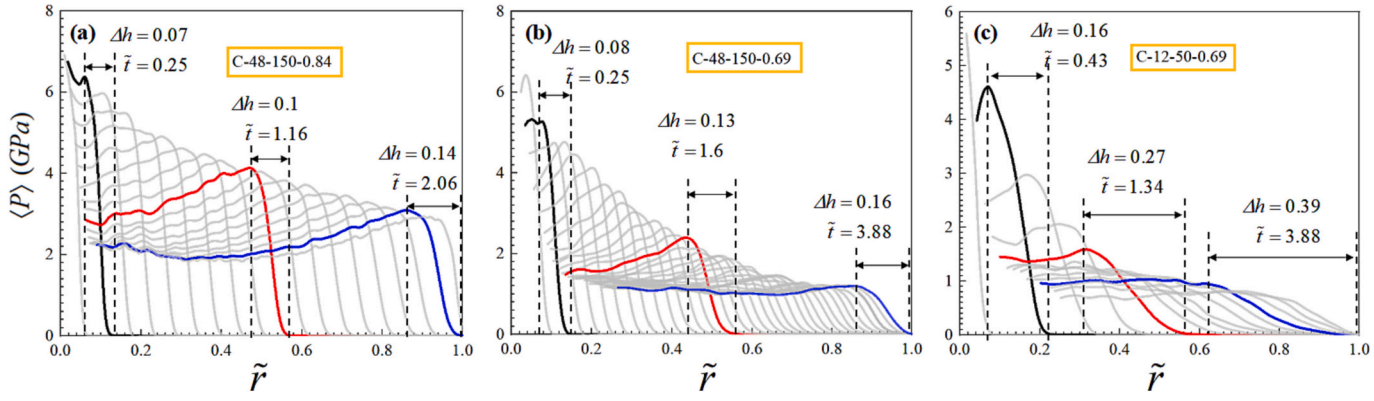

Fig. 14. Evolutions of the $\langle P \rangle(\tilde{r})$ profiles in systems C-48-150-0.69 (a), C-48-150-0.84 (b), and C-12-50-0.69 (c).

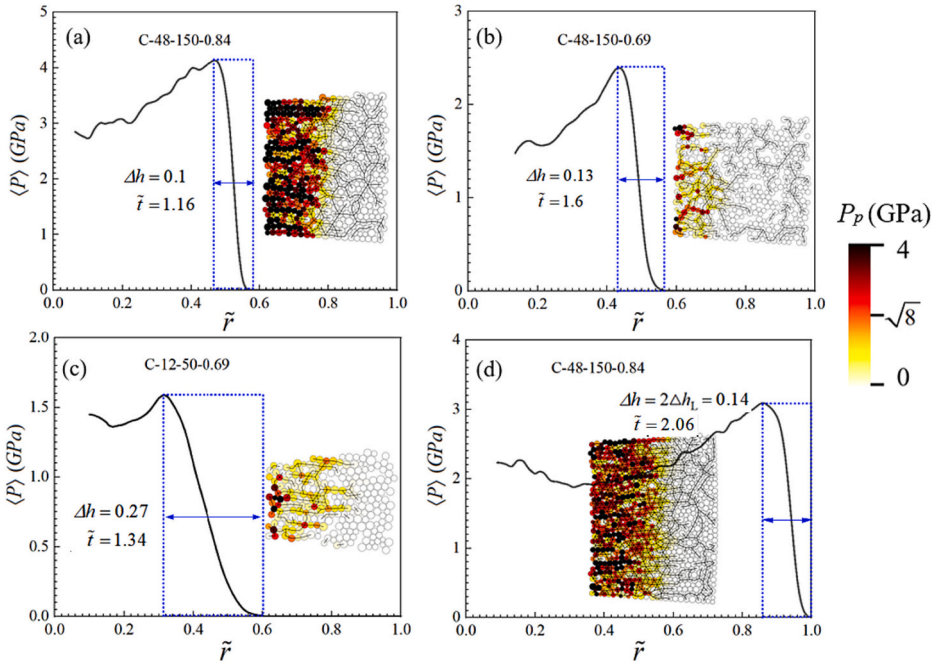

Fig. 15. Snapshots of parts of blast-loaded particle rings wherein particles are colored by their instantaneous quasistatic pressure, P_p, and the particles in contact with the contact force beyond a threshold are connected by lines in systems C-48-150-0.84, $\tilde{t} = 1.16$ (a), C-48-150-0.69, $\tilde{t} = 1.6$ (b), C-12-50-0.69, $\tilde{t} = 1.34$ (c) and C-48-150-0.84, $\tilde{t} = 2.06$ (d).

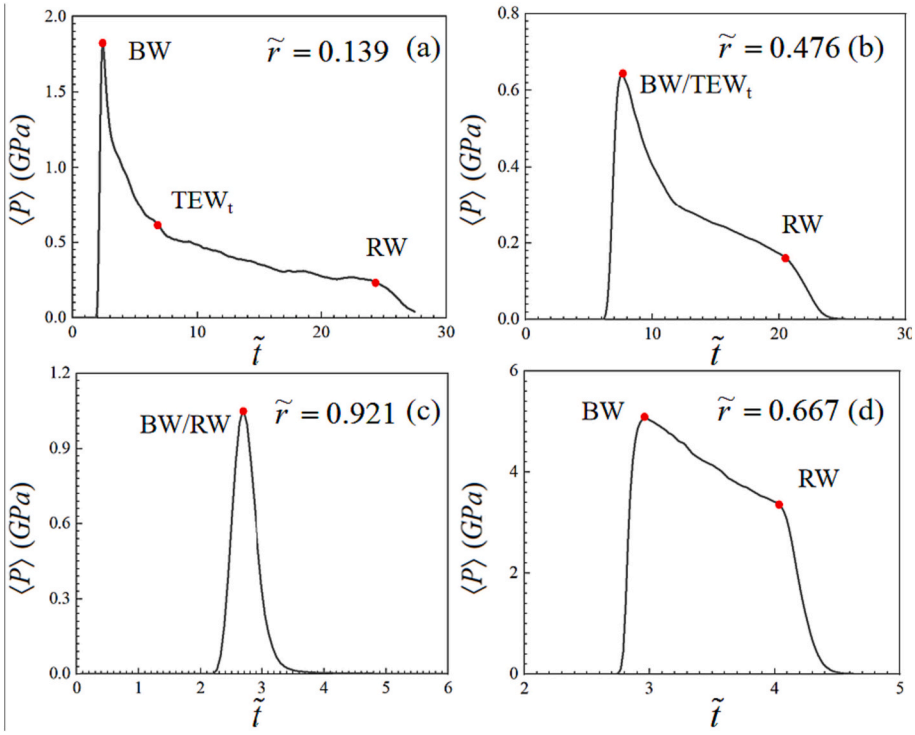

Fig. 16. Four typical $\langle P\rangle(\tilde{t})$ curves at locations affected by different waves in systems C-12-220-0.84 (a), C-12-220-0.84 (b), C-12-50-0.84 (b), and C-120-240-0.84 (d).

$$\tilde{R}_{\text{in,REW}_\text{h}} + \int_{\tilde{t}_{\text{REW}_\text{h},\text{in}}}^{\tilde{t}_{\text{RW}}} \tilde{V}_{\text{TEW}_\text{t}} d\tilde{t} + \int_{\tilde{t}_{\text{BW,out}}}^{\tilde{t}_{\text{RW}}} \tilde{V}_{\text{RW}} d\tilde{t} = 1 \qquad \text{if} \quad \tilde{r}_{\text{cr}} < 1 \text{ and } \tilde{t}_{\text{REW}_\text{h},\text{in}} < \tilde{t}_{\text{SSW,in}} \tag{6}$$

The second constraint in Eq. (6), namely, $\tilde{t}_{\text{REW}_\text{h},\text{in}} < \tilde{t}_{\text{SSW,in}}$, requires the onset of the TEW_t to be earlier than the reflection off the inner surface of the RW, which leads to a second threshold of the outer radius, $R^{\text{I}}_{\text{out,th}}$. For the particle ring/shell with $R_{\text{out},0}$ smaller than $R^{\text{I}}_{\text{out,th}}$, the $\langle P\rangle(\tilde{t})$ profiles throughout the thickness of the ring/shell remain self-similar, i.e., composed of a singular pressure peak, as shown in Fig. 16 (d). Assuming the BW and RW propagate at constant velocities approximated by their average velocities in particle ring/shell with

$R^{II}_{out,th}$, $\widetilde{V}_{BW}(\tilde{t}) \sim \widetilde{\overline{V}}_{BW,th}$, $\widetilde{V}_{RW}(\tilde{t}) \sim \widetilde{\overline{V}}_{RW,th}$, the criterion $\tilde{t}_{REW_h,in} = \tilde{t}_{SSW,in}$ with regard to the $R^{I}_{out,th}$ can be formulated as

$$\tilde{t}_{REW_h,in} - \tilde{t}_{DW,in} = \frac{1}{\widetilde{\overline{V}}_{BW,th}} + \frac{R^{II}_{out,th} - R_{in,REW_h}}{\left(R^{II}_{out,th} - R_{in,0}\right)\widetilde{\overline{V}}_{RW,th}} \tag{7}$$

which yields the expression of the $R^{I}_{out,th}$

$$R^{II}_{out,th} = \frac{\left(\tilde{t}_{REW_h,in} - \tilde{t}_{DW,in}\right)\widetilde{\overline{V}}_{BW,th}\widetilde{\overline{V}}_{RW,th}R_{in,0} - \widetilde{\overline{V}}_{RW,th}R_{in,0} - \widetilde{\overline{V}}_{BW,th}R_{in,REW_h}}{\left(\tilde{t}_{REW_h,in} - \tilde{t}_{DW,in}\right)\widetilde{\overline{V}}_{BW,th}\widetilde{\overline{V}}_{RW,th} - \widetilde{\overline{V}}_{RW,th} - \widetilde{\overline{V}}_{BW,th}} \tag{8}$$

The estimation of $\widetilde{\overline{V}}_{BW,th}$ and $\widetilde{\overline{V}}_{RW,th}$ is presented in Appendix II. Table 2 presents the dimensionless $R^{I}_{out,th}$ and $R^{II}_{out,th}$ for all numerical systems scaled by $R_{in,0}$, $\widetilde{\overline{R}}^{I}_{out,th} = R^{I}_{out,th}/R_{in,0}$, $\widetilde{\overline{R}}^{II}_{out,th} = R^{II}_{out,th}/R_{in,0}$. f_0 and $R_{in,0}$ have opposite effects on $\widetilde{\overline{R}}^{I}_{out,th}$ and $\widetilde{\overline{R}}^{II}_{out,th}$, both of which increase with f_0 and decrease with $R_{in,0}$. The spherical configuration entails larger $\widetilde{\overline{R}}^{I}_{out,th}$ and $\widetilde{\overline{R}}^{II}_{out,th}$ compared with the cylindrical configuration with the same $R_{in,0}$ and equivalent f_0.

Fig. 17 schematizes the evolution of $\langle P\rangle(\tilde{t})$ profiles in systems with increasing particle ring/shell thickness alongside the corresponding $\tilde{r}$-$\tilde{t}$ diagrams of the wave systems. For the particle ring/shell with $\widetilde{\overline{R}}_{out,0} > \widetilde{\overline{R}}^{I}_{out,th}$, the pressure histories $\langle P\rangle(\tilde{t})$ in the annular regions extending from $\tilde{r}=1$ to either $\tilde{r} = \tilde{r}_{RW}$ (if $\widetilde{\overline{R}}^{I}_{out,th} < \widetilde{\overline{R}}_{out,0} \le \widetilde{\overline{R}}^{II}_{out,th}$) or $\tilde{r} = \tilde{r}_{cr}$ (if $\widetilde{\overline{R}}_{out,0} > \widetilde{\overline{R}}^{II}_{out,th}$) display a three-phase profile defined by two characteristic pressures $\langle P_{peak}\rangle$ and $\langle P_{TEW_t}\rangle$ and two timescales $D\tilde{t}_I$ and $D\tilde{t}_{II}$, as denoted in Fig. 16. Here, $\langle P_{TEW_t}\rangle$ is the plateau pressure after the unloading of the TEW, and $D\tilde{t}_I$ and $D\tilde{t}_{II}$ are the durations of the initial pressure peak and the ensuing pressure plateau, respectively. The $\langle P\rangle(\tilde{t})$ profiles in the annular region $\tilde{r} > \tilde{r}_{cr}$ in the particle ring/shell with $\widetilde{\overline{R}}_{out,0} > \widetilde{\overline{R}}^{II}_{out,th}$ are primarily composed of the pressure plateau; therefore, only $\langle P_{TEW_t}\rangle$ and $D\tilde{t}_{II}$ are relative. Note that $\langle P_{TEW_t}\rangle$ is identical to $\langle P_{peak}\rangle$ in the region $\tilde{r} > \tilde{r}_{cr}$. In the particle ring/shell with $\widetilde{\overline{R}}_{out,0} \le \widetilde{\overline{R}}^{II}_{out,th}$ or the outer annular region ($\tilde{r} > \tilde{r}_{RW}$) in the particle ring/shell with $\widetilde{\overline{R}}^{I}_{out,th} < \widetilde{\overline{R}}_{out,0} \le \widetilde{\overline{R}}^{II}_{out,th}$, the $\langle P\rangle(\tilde{t})$ profiles feature a prominent pressure peak defined by $\langle P_{TEW_t}\rangle$ and the duration $D\tilde{t}_{III}$.

Since various $\langle P\rangle(\tilde{t})$ profiles are characterized by two characteristic pressures, $\langle P_{peak}\rangle$ and $\langle P_{TEW_t}\rangle$, and three characteristic times, $D\tilde{t}_I$, $D\tilde{t}_{II}$ and $D\tilde{t}_{III}$, knowledge about their variations with propagation distance, $\tilde{r}$, enables us to reproduce the loading histories exerted on particles at different distances from the inner surface in particle rings/shells with varied thicknesses. Fig. 12(a) presents the decay of $\langle P_{peak}\rangle$ with $\tilde{r}$, which varies with f_0 and $R_{in,0}$. The decay of $\langle P_{TEW_t}\rangle$ with $\tilde{r}$ shown in Fig. 12(c) is much milder, almost flattening in most densely packed particle rings. Noticeably, the $\langle P_{TEW_t}\rangle(\tilde{r})$ curve collapses with the $\langle P_{peak}\rangle(\tilde{r})$ curve beyond $\tilde{r} = \tilde{r}_{cr}$ (see the inset in Fig. 12(c)). The variations in $D\tilde{t}_I$, $D\tilde{t}_{II}$ and $D\tilde{t}_{III}$ with $\tilde{r}$ can be deduced from the arrival time intervals between the pertinent waves.

$$\text{for } \tilde{r} \le \tilde{r}_{RW} \text{ if } \widetilde{\overline{R}}^{I}_{out,th} \le \widetilde{\overline{R}}_{out,0} < \widetilde{\overline{R}}^{II}_{out,th} \text{ and } \tilde{r} \le \tilde{r}_{cr} \text{ if } \widetilde{\overline{R}}_{out,0} \ge \widetilde{\overline{R}}^{II}_{out,th} \quad \Delta\tilde{t}_I(\tilde{r}) = \tilde{t}_{TEW_t}(\tilde{r}) - \tilde{t}_{BW}(\tilde{r}) \tag{9}$$

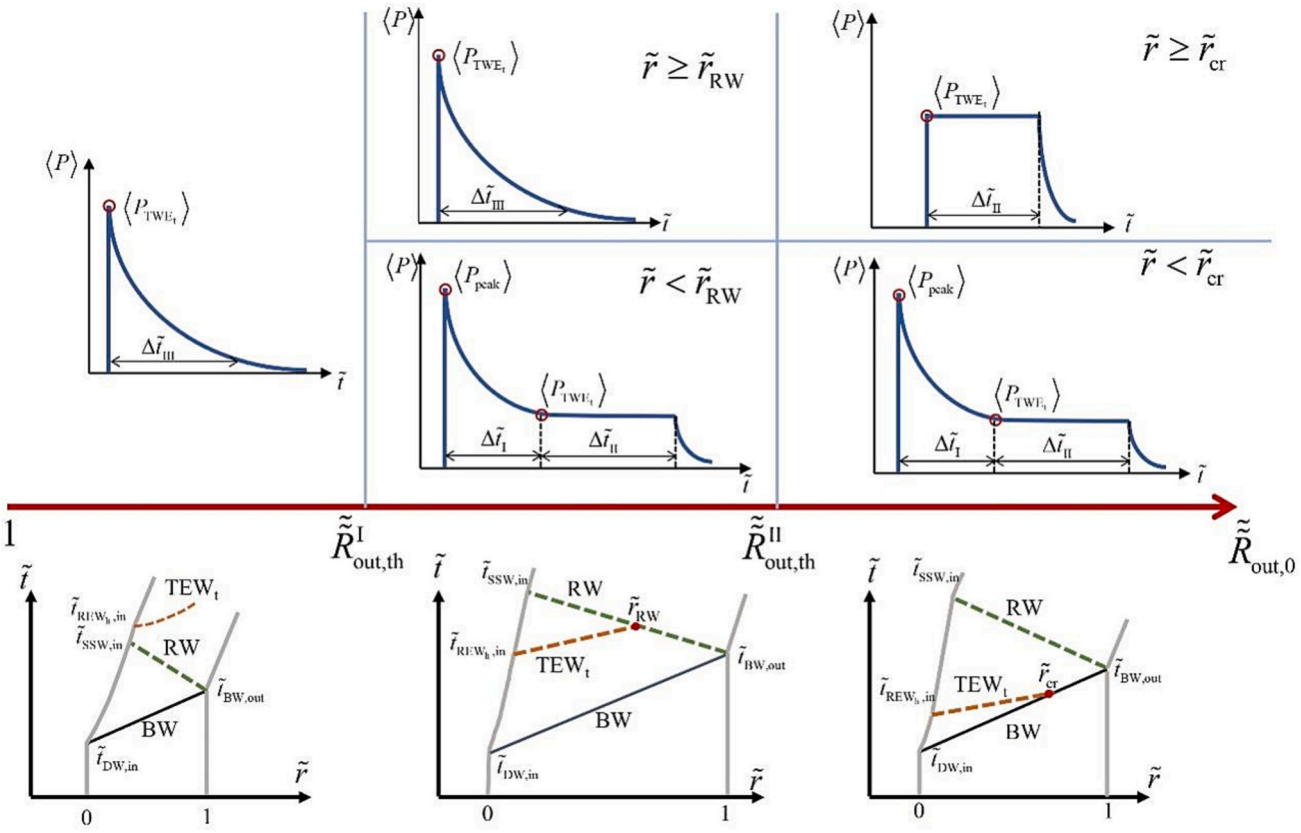

Fig. 17. Schematics of the distinct $\langle P\rangle(\tilde{t})$ profiles affected by the different waves in the particle ring/shell with increasing thickness. Bottom row: characteristic $\tilde{r}$-$\tilde{t}$ diagrams of the wave systems corresponding to the particle/ring with thicknesses in the range $1 < \widetilde{\overline{R}}_{out,0} \le \widetilde{\overline{R}}^{I}_{out,th}$, $\widetilde{\overline{R}}^{I}_{out,th} < \widetilde{\overline{R}}_{out,0} \le \widetilde{\overline{R}}^{II}_{out,th}$ and $\widetilde{\overline{R}}_{out,0} > \widetilde{\overline{R}}^{II}_{out,th}$.

$$\begin{aligned}&\text{for } \widetilde{r} \le \widetilde{r}_{\mathrm{RW}} \text{ if } \widetilde{\widetilde{R}}^{\mathrm{I}}_{\mathrm{out,th}} \le \widetilde{\widetilde{R}}_{\mathrm{out},0} < \widetilde{\widetilde{R}}^{\mathrm{II}}_{\mathrm{out,th}} \text{ or } \widetilde{r} \le \widetilde{r}_{\mathrm{cr}} \text{ if } \widetilde{\widetilde{R}}_{\mathrm{out},0} \ge \widetilde{\widetilde{R}}^{\mathrm{II}}_{\mathrm{out,th}}\\ &\Delta\widetilde{t}_{\mathrm{II}}(\widetilde{r}) = \widetilde{t}_{\mathrm{RW}}(\widetilde{r}) - \widetilde{t}_{\mathrm{TEW_t}}(\widetilde{r})\\ &\text{for } \widetilde{r} > \widetilde{r}_{\mathrm{cr}} \text{ if } \widetilde{\widetilde{R}}_{\mathrm{out},0} \ge \widetilde{\widetilde{R}}^{\mathrm{II}}_{\mathrm{out,th}}\\ &\Delta\widetilde{t}_{\mathrm{II}}(\widetilde{r}) = \widetilde{t}_{\mathrm{RW}}(\widetilde{r}) - \widetilde{t}_{\mathrm{BW}}(\widetilde{r})\end{aligned} \tag{10}$$

$$\begin{aligned}&\text{for } \widetilde{r} > \widetilde{r}_{\mathrm{RW}} \text{ if } \widetilde{\widetilde{R}}^{\mathrm{I}}_{\mathrm{out,th}} \le \widetilde{\widetilde{R}}_{\mathrm{out},0} < \widetilde{\widetilde{R}}^{\mathrm{II}}_{\mathrm{out,th}} \text{ or if } \widetilde{\widetilde{R}}_{\mathrm{out},0} < \widetilde{\widetilde{R}}^{\mathrm{I}}_{\mathrm{out,th}}\\ &\Delta\widetilde{t}_{\mathrm{III}}(\widetilde{r}) = \widetilde{t}_{\mathrm{RW}}(\widetilde{r}) - \widetilde{t}_{\mathrm{BW}}(\widetilde{r})\end{aligned} \tag{11}$$

where $\widetilde{t}_{\mathrm{BW}}(\widetilde{r})$, $\widetilde{t}_{\mathrm{TEW_t}}(\widetilde{r})$ and $\widetilde{t}_{\mathrm{RW}}(\widetilde{r})$ are the times at which the BW, $\mathrm{TEW_t}$ and RW reach $\widetilde{r}$, clearly $\widetilde{t}_{\mathrm{BW}}(\widetilde{r}=0)=\widetilde{t}_{\mathrm{DW,in}}$, $\widetilde{t}_{\mathrm{BW}}(\widetilde{r}=1)=\widetilde{t}_{\mathrm{RW}}(\widetilde{r}=1)=\widetilde{t}_{\mathrm{BW,out}}$, $\widetilde{t}_{\mathrm{TEW_t}}(\widetilde{r}=0)=\widetilde{t}_{\mathrm{REW_h,in}}$, and $\widetilde{t}_{\mathrm{RW}}(\widetilde{r}=0)=\widetilde{t}_{\mathrm{SSW,in}}$. Assuming that the BW, $\mathrm{TEW_t}$ and RW propagate at constant velocities that are approximated by their average velocities in the particle ring/shell with $R^{\mathrm{II}}_{\mathrm{out,th}}$, $\widetilde{V}_{\mathrm{BW}}(\widetilde{t}) \sim \widetilde{\widetilde{V}}_{\mathrm{BW,th}}$, $\widetilde{V}_{\mathrm{TEW_t}}(\widetilde{t}) \sim \widetilde{\widetilde{V}}_{\mathrm{TEW_t,th}}$, and $\widetilde{V}_{\mathrm{RW}}(\widetilde{t}) \sim \widetilde{\widetilde{V}}_{\mathrm{RW,th}}$, respectively, we then have

$$\widetilde{r} = \int_{\widetilde{t}_{\mathrm{DW,in}}}^{\widetilde{t}_{\mathrm{BW}}(\widetilde{r})} \widetilde{V}_{\mathrm{BW}} d\widetilde{t} \approx \widetilde{\widetilde{V}}_{\mathrm{BW,th}}\left(\widetilde{t}_{\mathrm{BW}}(\widetilde{r}) - \widetilde{t}_{\mathrm{DW,in}}\right) \tag{12}$$

$$\widetilde{r} - \widetilde{R}_{\mathrm{REW_h,in}} = \int_{\widetilde{t}_{\mathrm{REW_h,in}}}^{\widetilde{t}_{\mathrm{TEW_t}}(\widetilde{r})} \widetilde{V}_{\mathrm{TEW_t}} d\widetilde{t} \approx \widetilde{\widetilde{V}}_{\mathrm{TEW_t,th}}\left(\widetilde{t}_{\mathrm{TEW_t}}(\widetilde{r}) - \widetilde{t}_{\mathrm{REW_h,in}}\right) \tag{13}$$

$$1 - \widetilde{r} = \int_{\widetilde{t}_{\mathrm{BW,out}}}^{\widetilde{t}_{\mathrm{RW}}(\widetilde{r})} \widetilde{V}_{\mathrm{RW}} d\widetilde{t} \approx \widetilde{\widetilde{V}}_{\mathrm{RW,th}}\left(\widetilde{t}_{\mathrm{RW}}(\widetilde{r}) - \widetilde{t}_{\mathrm{BW,out}}\right) \tag{14}$$

Deriving $\widetilde{t}_{\mathrm{BW}}(\widetilde{r})$, $\widetilde{t}_{\mathrm{TEW_t}}(\widetilde{r})$ and $\widetilde{t}_{\mathrm{RW}}(\widetilde{r})$ from Eqs. (12)–(14) and substituting them and $\widetilde{t}_{\mathrm{BW,out}} = 1/\widetilde{\widetilde{V}}_{\mathrm{BW,th}}$ into Eqs. (9) and (11) lead to

$$\begin{aligned}&\text{for } \widetilde{r} \le \widetilde{r}_{\mathrm{RW}} \text{ if } \widetilde{\widetilde{R}}^{\mathrm{I}}_{\mathrm{out,th}} \le \widetilde{\widetilde{R}}_{\mathrm{out},0} < \widetilde{\widetilde{R}}^{\mathrm{II}}_{\mathrm{out,th}} \text{ and } \widetilde{r} \le \widetilde{r}_{\mathrm{cr}} \text{ if } \widetilde{\widetilde{R}}_{\mathrm{out},0} \ge \widetilde{\widetilde{R}}^{\mathrm{II}}_{\mathrm{out,th}}\\ &\Delta\widetilde{t}_{\mathrm{I}}(\widetilde{r}) = \frac{\widetilde{r} - \widetilde{R}_{\mathrm{REW_h,in}}}{\widetilde{\widetilde{V}}_{\mathrm{TEW_t,th}}} - \frac{\widetilde{r}}{\widetilde{\widetilde{V}}_{\mathrm{BW,th}}} + \widetilde{t}_{\mathrm{REW_h,in}} - \widetilde{t}_{\mathrm{DW,in}}\end{aligned} \tag{15}$$

$$\begin{aligned}&\text{for } \widetilde{r} \le \widetilde{r}_{\mathrm{RW}} \text{ if } \widetilde{\widetilde{R}}^{\mathrm{I}}_{\mathrm{out,th}} \le \widetilde{\widetilde{R}}_{\mathrm{out},0} < \widetilde{\widetilde{R}}^{\mathrm{II}}_{\mathrm{out,th}} \text{ or } \widetilde{r} \le \widetilde{r}_{\mathrm{cr}} \text{ if } \widetilde{\widetilde{R}}_{\mathrm{out},0} \ge \widetilde{\widetilde{R}}^{\mathrm{II}}_{\mathrm{out,th}}\\ &\Delta\widetilde{t}_{\mathrm{II}}(\widetilde{r}) = \frac{1-\widetilde{r}}{\widetilde{\widetilde{V}}_{\mathrm{RW,th}}} - \frac{\widetilde{r} - \widetilde{R}_{\mathrm{REW_h,in}}}{\widetilde{\widetilde{V}}_{\mathrm{TEW_t,th}}} + \frac{1}{\widetilde{\widetilde{V}}_{\mathrm{BW,th}}} - \widetilde{t}_{\mathrm{REW_h,in}}\\ &\text{for } \widetilde{r} > \widetilde{r}_{\mathrm{cr}} \text{ if } \widetilde{\widetilde{R}}_{\mathrm{out},0} \ge \widetilde{\widetilde{R}}^{\mathrm{II}}_{\mathrm{out,th}}\\ &\Delta\widetilde{t}_{\mathrm{II}}(\widetilde{r}) = \frac{1-\widetilde{r}}{\widetilde{\widetilde{V}}_{\mathrm{RW,th}}} + \frac{1-\widetilde{r}}{\widetilde{\widetilde{V}}_{\mathrm{BW,th}}} - \widetilde{t}_{\mathrm{DW,in}}\end{aligned} \tag{16}$$

$$\begin{aligned}&\text{for } \widetilde{r} > \widetilde{r}_{\mathrm{RW}} \text{ if } \widetilde{\widetilde{R}}^{\mathrm{I}}_{\mathrm{out,th}} \le \widetilde{\widetilde{R}}_{\mathrm{out},0} < \widetilde{\widetilde{R}}^{\mathrm{II}}_{\mathrm{out,th}} \text{ or if } \widetilde{\widetilde{R}}_{\mathrm{out},0} < \widetilde{\widetilde{R}}^{\mathrm{I}}_{\mathrm{out,th}}\\ &\Delta\widetilde{t}_{\mathrm{III}}(\widetilde{r}) = \frac{1-\widetilde{r}}{\widetilde{\widetilde{V}}_{\mathrm{RW,th}}} + \frac{1-\widetilde{r}}{\widetilde{\widetilde{V}}_{\mathrm{BW,th}}} - \widetilde{t}_{\mathrm{DW,in}}\end{aligned} \tag{17}$$

Fig. 17 (a)-(c) exhibits plots of the $\Delta\widetilde{t}_{\mathrm{I}}(\widetilde{r})$, $\Delta\widetilde{t}_{\mathrm{II}}(\widetilde{r})$ and $\Delta\widetilde{t}_{\mathrm{II}}(\widetilde{r})$ predicted by Eqs. (15)–(17) in particle rings/shells with thicknesses in distinct ranges. The parameters in Eqs. (15)–(17), $\widetilde{\widetilde{V}}_{\mathrm{BW,th}}$, $\widetilde{\widetilde{V}}_{\mathrm{TEW_t,th}}$, $\widetilde{\widetilde{V}}_{\mathrm{RW,th}}$, $\widetilde{t}_{\mathrm{DW,in}}$, $\widetilde{t}_{\mathrm{REW_h,in}}$, and $\widetilde{R}_{\mathrm{in,TEW_t}}$ are derived from the simulation results in four typical systems, C-12-X-0.84, C-48-X-0.84, C-48-X-0.52 and S-12-X-0.69. The scatter data representing the simulation results are consistent with the trend lines predicted by Eqs. (15)–(17).

6. Discussion

Although the particle phase dynamic pressure, P_{d}, in the regions adjacent to the central charge is negligible compared with its quasistatic counterpart, P, which is the case in the simulations studied here, P_{d} is an integral part of the overall pressure, especially in the regions far away from the center charge or in the scenario involving modest blast loading. Correlated with the inertia of particles, P_{d} is not as sensitive to the evolution of the gaseous pressure exerted on the inner surface, P_{in}, as the quasistatic pressure P is, which gives rise to the contrast between the distinct decay laws of $P_{\mathrm{d,peak}}$ and P_{peak} (see Fig. 12 (a) and (b)). In this section, we attempt to establish a blast compaction model based on the continuum approximation to predict the kinetic energy imparted to the particle rings during the propagation of the BW, thereby accounting for the decay of $P_{\mathrm{d,peak}}$ with the propagation distance of the BW.

The schematic representation of the geometry considered in the model is shown in Fig. 18, wherein a BW with a sharp front propagates at a velocity of V_{BW}. The packing fraction jumps from f_0 to f_{comp} across the BW, while the particles about to be compacted by the BW gain the velocity of $u_{\mathrm{comp}}(R_{\mathrm{BW}})$, where R_{BW} is the radius of the BW. In a cylindrical geometry, mass conservation in the annular compacted band requires the particle velocity and acceleration, $u_{\mathrm{comp}}(R)$ and $\dot{u}_{\mathrm{comp}}(R)$, to satisfy Eqs. (18) and (19), respectively.

$$u_{\mathrm{comp}}(R) = \frac{V_{\mathrm{in}}R_{\mathrm{in}}}{R} \tag{18}$$

$$\dot{u}_{\mathrm{comp}}(R) = \frac{\dot{V}_{\mathrm{in}}R_{\mathrm{in}}}{R} + \frac{V_{\mathrm{in}}^2}{R} - \frac{(V_{\mathrm{in}}R_{\mathrm{in}})^2}{R^3} \tag{19}$$

where V_{in} and R_{in} are the instantaneous velocity and radius of the inner surface, respectively. Note that V_{in} is set by the particle velocity herein, $V_{\mathrm{in}} = u_{\mathrm{comp}}(R_{\mathrm{in}})$. Upon the BW

$$u_{\mathrm{comp}}(R_{\mathrm{BW}}) = \frac{V_{\mathrm{in}}R_{\mathrm{in}}}{R_{\mathrm{BW}}} \tag{20}$$

$$\dot{u}_{\mathrm{comp}}(R_{\mathrm{BW}}) = \frac{\dot{V}_{\mathrm{in}}R_{\mathrm{in}}}{R_{\mathrm{BW}}} + \frac{V_{\mathrm{in}}^2}{R_{\mathrm{BW}}} - \frac{V_{\mathrm{in}}^2R_{\mathrm{in}}^2}{R_{\mathrm{BW}}^3} \tag{21}$$

The V_{BW} and V_{in} must meet the Rankine-Hugoniot condition

$$V_{\mathrm{in}} = \frac{V_{\mathrm{BW}}R_{\mathrm{BW}}}{R_{\mathrm{in}}}\left(1 - \frac{\phi_0}{\phi_{\mathrm{comp}}}\right) \tag{22}$$

The momentum balance of the annular compacted band demonstrated in Fig. 18 is given by Eq. (23)

$$\begin{aligned}&\rho_p\phi_{comp}\int_{R_{in}(t)}^{R_{BW}(t)} \dot{u}_{comp}(R)RdR = -\rho_p\phi_0 u_{comp}(R_{BW})V_{\mathrm{BW}}R_{\mathrm{BW}}\\ &+\rho_p\phi_{comp}\int_{R_{in}(t)}^{R_{BW}(t)} F_{\nabla P}(R)\cdot RdR + \rho_p\phi_{comp}\int_{R_{in}(t)}^{R_{BW}(t)} F_{drag}(R)\cdot RdR\end{aligned} \tag{23}$$

where r_{p} is the material density of the particle, $r_{\mathrm{p}} = 2700\ \mathrm{kg/m^3}$, and $F_{\nabla P}$ and F_{drag} (units N/kg) are the pressure gradient forces and drag forces across the thickness of the annular compacted particle band, respectively, which are established by the diffusional pressure field. The first term on the R.H.S. of Eq. (23) arises from the growing mass of the compacted band. The second and third terms on the R.H.S. of Eq. (23) represent the total pressure gradient force and the total drag force exerted on the compacted band with a unit cross-sectional area. Notably, the continuum blast compaction model couples the pressure diffusion driven by gas infiltration with particle dynamics, which is absent in the numerical simulations. In contrast, in the FEM-DEM simulations, the coupling between the particles and the detonation products is mediated by the interaction between the outermost FEM meshes of the detonation products and the innermost layer of particles.

As a first-order estimation, we assume a linear pressure gradient across the thickness of the compacted band

$$F_{\nabla P} = -\frac{\nabla P}{\rho_p} = \frac{P_{in}}{\rho_p(R_{BW} - R_{in})} \tag{24}$$

where P_{in} is the instantaneous pressure exerted on the inner surface.

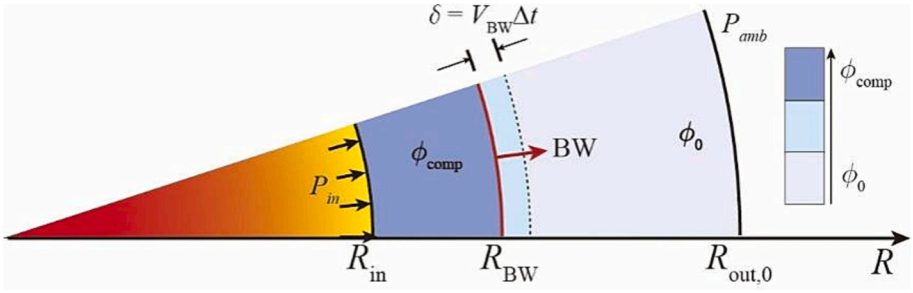

Fig. 18. Schematic representation of the wedge volumetric element with unit cross-sectional area taken into consideration in the blast compaction model.

Since the flow velocity relative to the particles depends on the local pressure gradient dictated by the Darcy and Forchheimer laws [41], F_{drag} is proportionate to $F_{\nabla P}$, as given in Eq. (25)

$$F_{drag} = \frac{1-\phi_p}{\phi_p} F_{\nabla P} = -\frac{1-\phi_p}{\phi_p}\frac{\nabla P}{\rho_p} = \frac{1-\phi_p}{\phi_p}\frac{P_{in}}{\rho_p (R_{BW}-R_{in})} \tag{25}$$

Substituting Eqs. (24)–(25) and (38) into Eq. (23) yields

$$\dot{V}_{in}(R_{BW}-R_{in}) + V_{in}^2\left[\frac{R_{BW}}{R_{in}} + \frac{\phi_{comp}}{\phi_{comp}-\phi_0}\frac{R_{in}}{R_{BW}} - 2\right] = \frac{P_{in}}{\phi_{comp}\rho_p}\frac{1}{2}\left(\frac{R_{BW}}{R_{in}}+1\right) \tag{26}$$

Eq. (26) describes the evolution of $\dot{V}_{in}$ with the initial condition of $\dot{V}_{in}=0$ and $R_{BW}=R_{in}$ at $t=0$. The integration of $\dot{V}_{in}$ gives rise to V_{in} and V_{BW} (Eq. (22)), whose integrations in turn yield R_{in} and R_{BW}. Note that P_{in} dramatically evolves due to the wave dynamics and the expansion of detonation products, which is difficult to model properly. Instead, we employ the simulation-derived $P_{in}(R_{in})$ curves, as shown in Fig. 13 (b), as the imposed unsteady boundary condition. Additionally, f_{comp} is the average over the thickness of the blast-compacted band since the actual f_{comp} profile peaks upon the front of the BW and undergoes a modest decrease affected by the TEW. Eqs. (18)–(26) constitute the complete formulations of the blast compaction model, which can be solved numerically, as elaborated in Appendix III.

Fig. 19 plots the analytically predicted trajectories of the inner and outer surfaces of rings, $\widetilde{R}_{in}^{pre}$ and the BW, $\widetilde{R}_{BW}^{pre}$, as well in systems C-48-150-0.52 (a), C-48-150-0.69 (b), and C-48-150-0.84 (c). The simulation-derived trajectories, $\widetilde{R}_{in}^{num}$, $\widetilde{R}_{out}^{num}$ and $\widetilde{R}_{BW}^{num}$, are superimposed in Fig. 19, showing good agreement. This substantiates the reliability of the blast compaction model in predicting the kinetic energy impacted into the particle ring/shell from the central detonation products. Keeping in mind the difference in the gas-particle coupling modeled in the simulations and the analytical model, the consistency shown in Fig. 19 justifies the simplification of gas-particle coupling in the simulations, which does not take into account the gas infiltration process. The predicted $\widetilde{R}_{in}^{pre}$ and $\widetilde{R}_{BW}^{pre}$ trajectories start to deviate from the $\widetilde{R}_{in}^{num}$ and $\widetilde{R}_{BW}^{num}$ curves when the BW propagates half way through the thickness of the ring, especially in the systems with small f_0 and $R_{in,0}$. This is mainly due to the decrease in f_0 by the TEW, which is not accounted for in the blast compaction model.

Based on the momentum obtained by the particles swept by the BW, the dynamic pressure at the BW is estimated by

$$P_{d,BW} = \rho_p \phi_{comp} V_{BW} u_{comp}(R_{BW}) \tag{27}$$

Substituting Eq. (20) into Eq. (27), we have

$$P_{d,BW} = \rho_p \phi_{comp} V_{BW} V_{in}\frac{R_{in}}{R_{BW}} \tag{28}$$

The variations in $P_{d,BW}$ with $\tilde{r}$ predicted by Eq. (28) in systems whose trajectories of characteristic features are shown in Fig. 19 are presented in Fig. 20, which are fitted well by power law functions. In accordance with the f_0 and $R_{in,0}$ dependences of the $\langle P_{d,peak}\rangle(\tilde{r})$ curves shown in Fig. 12(b), the analytically predicted dynamic pressure, $P_{d,BW}$, is higher in the particle ring/shell with smaller f_0 and $R_{in,0}$. Unlike the sharp front of the BW with a zero front width assumed in the blast compaction model, the blast front has a finite width, Dw, as revealed by the simulations. Since particles within the width of the blast front are subjected to markedly varied stresses due to the heterogeneous network of force chains, the dynamic pressure at the blast front should be averaged over the Dw

$$\overline{\left\langle P_{d,BW}^{num}\right\rangle} = \frac{\sum_i d_{p,i}^2 P_{d,i}}{4\left[\left(R_{BW}^{+}\right)^2 - \left(R_{BW}^{-}\right)^2\right]} \tag{29}$$

where $d_{p,i}$ and $P_{d,i}$ are the diameter and the dynamic pressure of particle i positioned inside the width of the blast front, respectively, R_{BW}^{+} and R_{BW}^{-} are the radii of the beginning and ending points of the blast front,

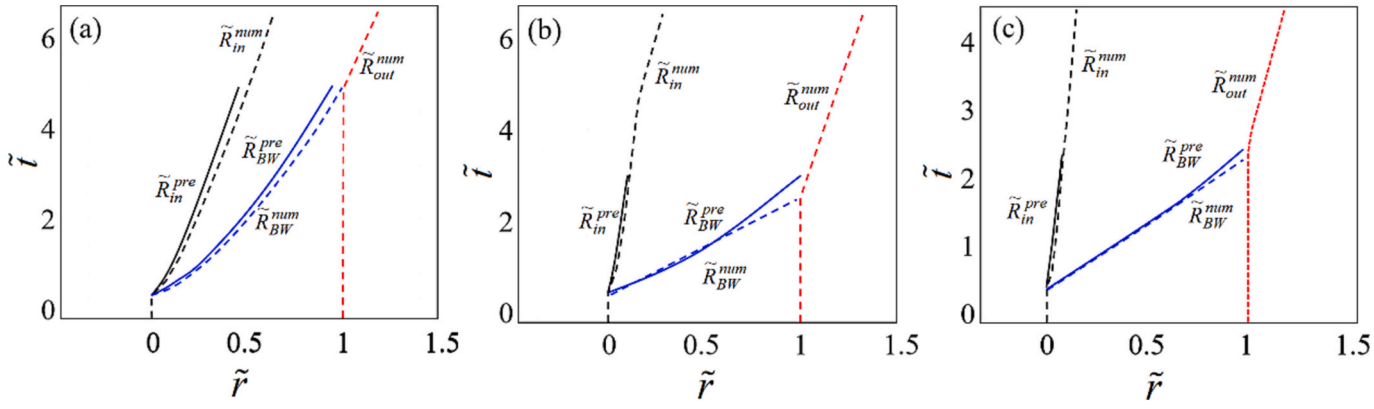

Fig. 19. Comparisons of the trajectories of the inner and outer surfaces, the BW derived from the simulations and the analytical predictions in systems C-48-150-0.52 (a), C-48-150-0.84 (b), and C-12-50-0.84 (c).

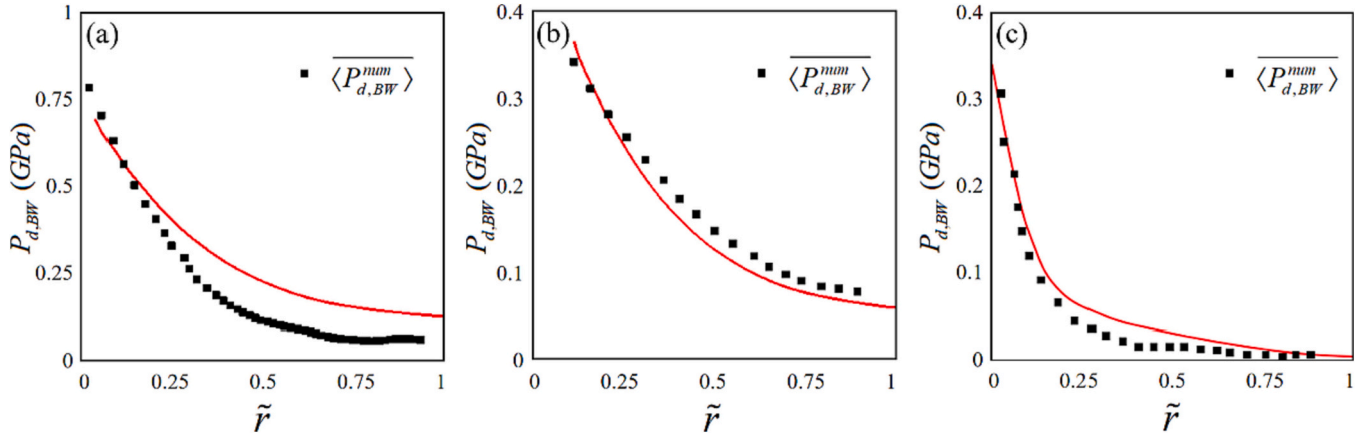

Fig. 20. Variations in the dynamic pressure at the BW with $\tilde{r}$ derived from the blast compaction model and the simulations, $P_{d,BW}(\tilde{r})$ and $\overline{\langle P_{d,BW}^{num} \rangle}(\tilde{r})$, in systems C-48-150-0.52 (a), C-48-150-0.84 (b), and C-12-50-0.84 (c).

respectively, $R_{BW} = (R_{BW}^{+}+R_{BW}^{-})/2$, and $Dw = R_{BW}^{+} - R_{BW}^{+}$. The numerically derived dynamic pressure at the blast front, $\overline{\langle P_{d,BW}^{num} \rangle}$, displays the same decaying trend as the predicted ones in various systems, as indicated in Fig. 20. The good agreement between the $P_{d,BW}(\tilde{r})$ and the $\overline{\langle P_{d,BW}^{num} \rangle}(\tilde{r})$ curves begins to worsen midway through the thickness of the ring, coinciding with the increasing deviation between $\tilde{R}_{in}^{pre}$ ($\tilde{R}_{BW}^{pre}$) and $\tilde{R}_{in}^{num}$ ($\tilde{R}_{BW}^{num}$). This is attributed to the dispersion of the BW. Specifically, the widening of the blast front means an increasing number of weakly compressed, slow moving particles are entrained into the blast front, resulting in a considerably lower $\overline{\langle P_{d,BW}^{num} \rangle}(\tilde{r})$ than the predicted one, $P_{d,BW}(\tilde{r})$.

The formulation given in Eq. (29) is the volume-averaged pressure, while the pressures analyzed in Section 5, either the quasistatic or dynamic pressure, are phase-averaged pressures. Evidently, the phase-averaged pressure is higher than the volume-averaged pressure. Neglecting the pressure in the interstitial gases, the proportionality between them is the volume fraction. The soil loading measured in the blast experiments and the underground or near ground structures is related to the volume-averaged dynamic pressure. Hence, the aforementioned $P_{d,BW}(\tilde{r})$ and $\overline{\langle P_{d,BW}^{num} \rangle}(\tilde{r})$ are more relevant with regard to blast prevention. On the other hand, the quasistatic pressure, P_s, arises from the deformation of the particle skeleton, which depends on the particle-scale structure and the constitutive relation of the materials composing particles. Hence, P_s is indicative of the elastic energy stored by the deformed particle skeleton. The time history of P_s, $P_s(t)$, is also the primary parameter governing the resultant particle fragmentation and fragmentation dissipated energy once P_s exceeds the fracture strength P_s of the particle. In addition to inelastic collisions between particles, the visa-plastic deformation and fragmentation of particles are the other two major energy dissipation processes taken into account in the present work. Therefore, the evolution of the quasistatic pressure field helps explain energy dissipation through particles subjected to blast loading.

7. Conclusion

In this study, we conducted FEM-DEM simulations using 2D cylindrical and 3D spherical stratified configurations to investigate the propagation of the blast wave (BW) in dry sand subjected to a shallow buried blast. Our research has yielded several key findings, which we outline below:

1. The granular dynamics in terms of the evolution of quasistatic and dynamic pressure fields are found to be governed by the complex wave system that arises from the coupling between the central detonation products and the enclosing particle ring/shell.
2. The coupling effect changes as the blast wave propagates, leading to a decrease of the propagation velocity. Therefore thicker ring/shells correspond to the slower blast propagation. With the M/C increasing fronm $O(10^1)$ to $O(10^2)$, the average blast wave velocity decreases by 22.2% and 15.4% in 2D and 3D configurations, respectively.
3. The initial volume fraction and the charge volume play a significant role in blast wave propagation. As the densely packed sand (f_0 = 0.84) becomes loose (f_0 = 0.52), the average velocity of the blast wave decreases by 42.6% and 39.1% in the 2D configurations with small (R_{in} = 12 mm) and large (R_{in} = 48 mm) charges, respectively.

CRediT authorship contribution statement

Chuanshan Zhang: Methodology, Data curation, Formal analysis, Writing – original draft. **Chun Feng:** Software. **Kun Xue:** Formal analysis, Writing – review & editing.

Declaration of Competing Interest

The authors declare that they have no known competing financial interests or personal relationships that could have appeared to influence the work reported in this paper.

Data availability

Data will be made available on request.

Acknowledgements

This work was supported by the State Key Laboratory of Explosive Science and Technology (Grant No. ZDKT23-01) and National Key Laboratory of Shock Wave and Detonation Physics (Grant No. JCKYS2022212003).

Appendix I Particle phase pressure from the contact forces

Here, the pressure $\overline{P}_p(r)$ is the internal pressure of the particle phase in the annular region of radius r and thickness $2dp$. The calculation method is as follows: First, the stress tensor defined on the particle is obtained by the contact force vector $\boldsymbol{f}$ between the discrete elements of the particles

$$\sigma_{ij}^{A} = \frac{1}{V^{A}} \sum_{c=1}^{K} l_i^c f_j^c \tag{30}$$

where V^{A} is the volume of particle A, K is the total number of particles in contact with particle A, c is the contact point on particle A, and l_i^c is the vector from contact point c to the center of particle A. f_j^c is the contact force at contact point c of particle A. The particle pressure P_p^A is obtained by the first-order invariant of the stress tensor

$$P_p^A = \frac{I_1}{3} = \frac{tr\boldsymbol{\sigma}}{3} = \frac{\sigma_1 + \sigma_2 + \sigma_3}{3} \tag{31}$$

The radius is r, and the average pressure in the annular area with a thickness of $2d_p$ is

$$\overline{P}_p(r) = \frac{\sum_i V_i P_p^i}{\sum_i V_i} \tag{32}$$

where V_i is the volume of particle i in the annular region. Notably, the denominator in Eqs. (19) is the volume of the particle phase in the annular region, not the volume of the entire annular region, and is therefore the $\overline{P}_p(r)$ particle phase pressure rather than the mixture pressure after phase averaging.

The propagation law $\overline{P}_p(r)$ of the explosion load in the particle phase discussed in this paper is the static pressure contributed by the contact extrusion between particles. For particulate bulk media with strong convection, the dynamic pressure caused by the particle flow flux is also an important part of the explosion load. P_p^d is used to represent the dynamic pressure related to the particle velocity, which is distinguished from the static pressure P_p defined in Eqs. (17)–(19). In a ring belt or spherical shell W with a radius of r and a thickness of Dr. The average dynamic pressure in the annular direction can be determined by Eq. (36).

$$P_p^d(r) = \frac{\sum_{i\in\Omega} m_i v_i^2}{V_\Omega} = \begin{cases} \dfrac{\sum_{i\in\Omega} \rho_{p,i} d_{p,i}^2 v_i^2}{8r\Delta r} & \text{for a 2D column charge} \\ \dfrac{\sum_{i\in\Omega} \rho_{p,i} d_{p,i}^3 v_i^2}{6r^2\Delta r} & \text{for a 3D spherical charge} \end{cases} \tag{33}$$

where $r_{p,i}$, $d_{p,i}$ and v_i are the density, diameter, and velocity of particle i in the ring band or spherical shell, respectively. When the density and particle size distribution of the particle material are unchanged, the dynamic pressure P_p^d is determined by the particle velocity. In this paper, the propagation law of dynamic pressure in granular media is discussed from the explosion compaction model of a continuous media ring shell and the influence of the charge structure parameters.

Appendix II Estimation of $\widetilde{\overline{V}}_{\mathrm{BW,th}}$ and $\widetilde{\overline{V}}_{\mathrm{RW,th}}$

Assuming that the BW and RW propagate at constant velocities approximated by their average velocities in the particle ring/shell, $\widetilde{\overline{V}}_{\mathrm{BW,th}}$ and $\widetilde{\overline{V}}_{\mathrm{RW,th}}$ can be estimated. We use linear functions to fit $\widetilde{R}_{BW}$(t) and $\widetilde{R}_{RW}$(t), respectively.

$$\widetilde{R}_{BW}(\widetilde{t}) = \frac{\widetilde{t} - \widetilde{t}_{DW,in}}{\widetilde{t}_{BW,out} - \widetilde{t}_{DW,in}} \widetilde{R}_{out,0} \quad \widetilde{t}_{DW,in} < \widetilde{t} < \widetilde{t}_{BW,out} \tag{34}$$

$$\widetilde{R}_{RW} = \frac{\widetilde{t}_{SSW,in} - \widetilde{t}}{\widetilde{t}_{SSW,in} - \widetilde{t}_{BW,out}} \widetilde{R}_{out,0} + \frac{\widetilde{t} - \widetilde{t}_{BW,out}}{\widetilde{t}_{SSW,in} - \widetilde{t}_{BW,out}} \widetilde{R}_{SSW,in} \quad \widetilde{t}_{BW,out} < \widetilde{t} < \widetilde{t}_{SSW,in} \tag{35}$$

The derivation of time on the left and right sides of the (4.63)–(4.65) equal sign yields the propagation velocity of the explosion compaction wave BW and the reflected sparse wave head RW in the particle phase, $\widetilde{\overline{V}}_{\mathrm{BW,th}}$ and $\widetilde{\overline{V}}_{\mathrm{RW,th}}$

$$\widetilde{\overline{V}}_{BW,th} = \frac{\widetilde{R}_{out,0}}{\widetilde{t}_{BW,out} - \widetilde{t}_{DW,in}} \tag{36}$$

$$\widetilde{\overline{V}}_{RW} = \frac{\widetilde{R}_{out,0} - \widetilde{R}_{SSW,in}}{\widetilde{t}_{SSW,in} - \widetilde{t}_{BW,out}} \tag{37}$$

Appendix III Numerical solutions for the theoretical models

We present the iterative algorithm for numerically solving the shock compaction model introduced in Section 6. The superscript j represents the jth

time step.

For the shock compaction model, the initial condition ($j = 0$) corresponds to the impingement of the incident shock on the internal surface of the ring. Thus, we have

$$R_{comp}^{0} = R_{in}^{0} \tag{38}$$

$$\dot{V}_{in}^{0} = 0 \tag{39}$$

Substituting Eqs. (38) and (39) into Eq. (26) leads to the initial velocity of the internal surface

$$V_{in}^{0} = \sqrt{\frac{P_{g,0} - P_0}{\rho_p} \frac{\phi_{comp}}{\phi_0(\phi_{comp} - \phi_0)}} \tag{40}$$

Substituting Eq. (40) into Eq. (22), we obtain the initial velocity of the compaction front

$$V_{comp}^{0} = \sqrt{\frac{(P_{g,0} - P_0)}{\rho_p} \frac{\phi_0}{\phi_{comp}(\phi_{comp} - \phi_0)}} \tag{41}$$

Below, we present the time-marching scheme for the shock compaction model. R_{in}^{j+1} (R_{comp}^{j+1}) is updated using R_{in}^{j} (R_{comp}^{j}) and V_{in}^{j} (V_{comp}^{j}), as described in Eq. (42) (Eq. (43)),

$$R_{in}^{j+1} = R_{in}^{j} + V_{in}^{j} \cdot \Delta t \tag{42}$$

$$R_{comp}^{j+1} = R_{comp}^{j} + V_{comp}^{j} \cdot \Delta t \tag{43}$$

where D*t* is a sufficiently small time interval estimated by the simulation-derived time it takes for the compaction front to reach the external surface. The interface pressure P_g in the particle ring is given by the pressure curve in the outermost explosive mesh in the simulation. Substituting R_{in}^{j+1}, R_{comp}^{j+1}, and V_{in}^{j} into Eq. (D9), we obtain the acceleration of the internal surface at the $j + 1$ time step, $\dot{V}_{in}^{j+1}$.

$$\dot{V}_{in}^{j+1} = \frac{1}{R_{comp}^{j+1} - R_{in}^{j+1}} \left[\frac{P_g^{j+1} - P_0}{2\phi_{comp}\rho_p} \left(\frac{R_{comp}^{j+1}}{R_{in}^{j+1}} + 1 \right) - \left(V_{in}^{j} \right)^2 \left(\frac{R_{comp}^{j+1}}{R_{in}^{j+1}} + \frac{\phi_{comp}}{\phi_{comp} - \phi_0} \frac{R_{in}^{j+1}}{R_{comp}^{j+1}} - 2 \right) \right] \tag{44}$$

which leads toV_{in}^{j+1}

$$V_{in}^{j+1} = V_{in}^{j} + \dot{V}_{in}^{j+1} \cdot dt \tag{45}$$

V_{comp}^{j+1} ought to satisfy the Rankine-Hugoniot condition (Eq. (22)) and be updated by Eq. (D11)

$$V_{comp}^{j+1} = \frac{V_{in}^{j+1} R_{in}^{j+1} \phi_{comp}}{R_{comp}^{j+1}(\phi_{comp} - \phi_0)}. \tag{46}$$

Eqs. (D5)–(D11) are solved iteratively until the compaction front arrives at the external surface, $R_{\mathrm{comp}}(t_{\mathrm{comp}}) = R_{\mathrm{out.0}}$, wherein t_{comp} represents the end time of the shock compaction model.

References

[1] L. Figuli, D. Cekerevac, C. Bedon, B. Leitner, L. Di Sarno, Numerical analysis of the blast wave propagation due to various explosive charges, Adv. Civ. Eng. 2020 (2020) 1–11.

[2] S.E. Rigby, S.D. Fay, A. Tyas, S.D. Clarke, J.J. Reay, J.A. Warren, M. Gant, I. Elgy, Influence of particle size distribution on the blast pressure profile from explosives buried in saturated soils, Shock Waves 28 (2017) 613–626.

[3] S.E. Rigby, S.D. Fay, S.D. Clarke, A. Tyas, J.J. Reay, J.A. Warren, M. Gant, I. Elgy, Measuring spatial pressure distribution from explosives buried in dry Leighton Buzzard sand, Int. J. Impact Eng. 96 (2016) 89–104.

[4] C. Hansen, R.Y.S. Pak, Centrifuge characterization of buried, explosive-induced soil ejecta kinematics and crater morphology, J. Dynam. Behav. Mater. 2 (2016) 306–325.

[5] J.D. Reinecke, F.J. Beetge, I. Horsfall, M. Miyambo, Partitioning of a scaled shallow-buried near-field blast load, in: 30th International Symposium on Shock Waves 2, 2017, pp. 1351–1356.

[6] M. Grujicic, B. Pandurangan, B.A. Cheeseman, The effect of degree of saturation of sand on detonation phenomena associated with shallow-buried and ground-laid mines, Shock. Vib. 13 (2006), 652405.

[7] D. Fiserova, Numerical Analysis of Buried Mine Explosions with Emphasis on Effect of Soil Properties on Loading, Cranfield University, Defence College of Management and Technology, 2006.

[8] M. Grujicic, R. Yavari, J. Snipes, S. Ramaswami, A combined finite-element/discrete-particle analysis of a side-vent-channel-based concept for improved blast-survivability of light tactical vehicles, Int. J. Struct. Integr. 7 (2016) 106–141.

[9] M. Grujicic, R. Yavari, S. Ramaswami, J. Snipes, Side-vent-channels solution for improved buried-mine-blast survivability of a light-tactical-vehicle, Int. J. Struct. Integr. 8 (2017) 108–133.

[10] E.C. Leong, S. Anand, H.K. Cheong, C.H. Lim, Re-examination of peak stress and scaled distance due to ground shock, Int. J. Impact Eng. 34 (2007) 1487–1499.

[11] J.P. Borg, T.J. Vogler, Mesoscale calculations of the dynamic behavior of a granular ceramic, Int. J. Solids Struct. 45 (2008) 1676–1696.

[12] J. Bakken, T. Slungaard, T. Engebretsen, S.O. Christensen, Attenuation of shock waves by granular filters, Shock Waves 13 (2003) 33–40.

[13] Q. Yuan, X. Kong, J. Zhang, Q. Fang, J. Hong, Three-dimensional mesoscopic modelling of shock wave propagation and attenuation in gravel granular filter, Powder Technol. 394 (2021) 838–852.

[14] M. Rahmani, A.N. Oskouei, A.M. Petrudi, Experimental and numerical study of the blast wave decrease using sandwich panel by granular materials core, Defence Technol. 17 (2021) 1660–1670.

[15] J. Li, K. Xue, J. Zeng, B. Tian, X. Guo, Shock-induced interfacial instabilities of granular media, J. Fluid Mech. 930 (2021).

[16] P. Han, K. Xue, C. Bai, Explosively driven dynamic compaction of granular media, Phys. Fluids 33 (2021).

[17] X. Yu, L. Chen, Q. Fang, J. Zhang, D. Guo, X. Hou, Determination of attenuation effects of coral sand on the propagation of impact-induced stress wave, Int. J. Impact Eng. 125 (2019) 63–82.

[18] M.H. Sadd, G. Adhikari, F. Cardoso, DEM simulation ofwave propagation in granular materials, Powder Technol. 109 (1) (2000) 222–233.

[19] V.S. Deshpande, R.M. McMeeking, H.N.G. Wadley, A.G. Evans, Constitutive model for predicting dynamic interactions between soil ejecta and structural panels, J. Mech. Phys. Solids 57 (2009) 1139–1164.

[20] Stefan Luding, Introduction to discrete element methods, Eur. J. Environ. Civ. Eng. 12 (2008) 785–826.

[21] S. Luding, M. Lätzel, W. Volk, S. Diebels, H.J. Herrmann, From discrete element simulations to a continuum model, Comput. Methods Appl. Mech. Eng. 191 (2001) 21–28.

[22] Q. Tang, N. Jiang, Y. Yao, C. Zhou, X. Luo, T. Wu, Safety assessment of buried gas pipeline subject to surface explosion: a case study in Wuhan, China, Eng. Fail. Anal. 120 (2021).
[23] M. Grujicic, B. Pandurangan, R. Qiao, B.A. Cheeseman, W.N. Roy, R.R. Skaggs, R. Gupta, Parameterization of the porous-material model for sand with different levels of water saturation, Soil Dyn. Earthq. Eng. 28 (2008) 20–35.
[24] G.D. Nguyen, I. Einav, The Energetics of Cataclasis Based on Breakage Mechanics, Mechanics, Structure and Evolution of Fault Zones, 2009, pp. 1693–1724.
[25] C.E. Anderson, T. Behner, C.E. Weiss, Mine blast loading experiments, Int. J. Impact Eng. 38 (2011) 697–706.
[26] A. Kyner, K. Dharmasena, K. Williams, V. Deshpande, H. Wadley, High intensity impulsive loading by explosively accelerated granular matter, Int. J. Impact Eng. 108 (2017) 229–251.
[27] T. Børvik, L. Olovsson, A.G. Hanssen, K.P. Dharmasena, H. Hansson, H.N. G. Wadley, A discrete particle approach to simulate the combined effect of blast and sand impact loading of steel plates, J. Mech. Phys. Solids 59 (2011) 940–958.
[28] H. Mo, F.-S. Lien, F. Zhang, D.S. Cronin, A mesoscale study on explosively dispersed granular material using direct simulation, J. Appl. Phys. 125 (2019).
[29] L. Olovsson, A.G. Hanssen, T. Børvik, M. Langseth, A particle-based approach to close-range blast loading, Europ. J. Mech. A/Solids 29 (2010) 1–6.
[30] K. Nosrati, S. Movahedirad, M.A. Sobati, Pressure wave attenuation in agas solid fluidized bed: effects of particles size, density and the electrostatic charge, Powder Technol. 326 (2018) 281–287.
[31] K. Xue, J. Liu, C. Feng, Y. Gan, C. Bai, Explosively driven hierarchical particle jetting, Chem. Eng. Sci. 202 (2019) 250–269.
[32] C. Feng, S. Li, B. Zhang, Numerical simulation on complete process of three-dimensional bench blasting in an open-pit mine based on CDEM, Explos. Shock Waves 39 (2) (2019), 024201-1-024201-11.
[33] C. Feng, S. Li, X. Liu, Semi-spring contact model and its application to failure simulation of slope, Chin. J. Theoret. Appl. Mech. 43 (1) (2011) 184–192.
[34] H. Wang, C. Bai, C. Feng, K. Xue, X. Zhu, An efficient CDEM-based method to calculate full-scale fragment field of warhead, Int. J. Impact Eng. 133 (2019).
[35] J. Loiseau, W. Georges, A.J. Higgins, Validation of the gurney model in planar geometry for a conventional explosive, Propell. Explosiv. Pyrotechn. 41 (2016) 655–664.
[36] A.M. Milne, Gurney analysis of porous shells, Propell. Explosiv. Pyrotechn. 41 (2016) 665–671.
[37] B. Mobaraki, M. Vaghefi, Numerical study of the depth and cross-sectional shape of tunnel under surface explosion, Tunn. Undergr. Space Technol. 47 (2015) 114–122.
[38] K. Bagi, Statistical analysis of contact force components in random granular assemblies, Granul. Matter 5 (2003) 45–54.
[39] Z. Cheng, J. Wang, Quantification of particle crushing in consideration of grading evolution of granular soils in biaxial shearing: a probability-based model, Int. J. Numer. Anal. Methods Geomech. 42 (2018) 488–515.
[40] J. de Bono, G. McDowell, Particle breakage criteria in discrete-element modelling, Géotechnique 66 (2016) 1014–1027.
[41] A. Britan, G. Ben-Dor, Shock tube study of the dynamical behavior of granular materials, Int. J. Multiphase Flow 32 (2006) 623–642.